ARTICLE

Dissecting and targeting noncanonical functions of EZH2 in multiple myeloma via an EZH2 degrader

Xufen Yu[1,6✉], Jun Wang[2,3,6], Weida Gong[2], Anqi Ma[1], Yudao Shen[1], Chengwei Zhang[1], Xijuan Liu[2], Ling Cai[2,4], Jing Liu[1], Gang Greg Wang[2,3,5✉] and Jian Jin[1✉]

Multiple myeloma (MM) is the second most common hematological malignancy with poor prognosis. Enhancer of zeste homolog 2 (EZH2) is the enzymatic subunit of polycomb repressive complex 2 (PRC2), which catalyzes trimethylation of histone H3 lysine 27 (H3K27me3) for transcriptional repression. EZH2 have been implicated in numerous hematological malignancies, including MM. However, noncanonical functions of EZH2 in MM tumorigenesis are not well understood. Here, we uncovered a noncanonical function of EZH2 in MM malignancy. In addition to the PRC2-mediated and H3K27me3-dependent canonical function, EZH2 interacts with cMyc and co-localizes with gene activation-related markers, promoting MM tumorigenesis in a PRC2- and H3K27me3-independent manner. Both canonical EZH2-PRC2 and noncanonical EZH2-cMyc complexes can be effectively depleted in MM cells by MS177, an EZH2 degrader we reported previously, leading to profound activation of EZH2-PRC2-associated genes and simultaneous suppression of EZH2-cMyc oncogenic nodes. The MS177-induced degradation of both canonical EZH2-PRC2 and noncanonical EZH2-cMyc complexes also reactivated immune response genes in MM cells. Phenotypically, targeting of EZH2's both canonical and noncanonical functions by MS177 effectively suppressed the proliferation of MM cells both in vitro and in vivo. Collectively, this study uncovers a new noncanonical function of EZH2 in MM tumorigenesis and provides a novel therapeutic strategy, pharmacological degradation of EZH2, for treating EZH2-dependent MM.

Oncogene; https://doi.org/10.1038/s41388-023-02618-5

INTRODUCTION

Multiple myeloma (MM) is a common and aggressive blood malignancy, characterized by abnormal proliferation and accumulation of monoclonal plasma cells in the bone marrow (BM) [1, 2]. MM is initiated from a premalignant lesion called monoclonal gammopathy of undetermined significance (MGUS), and subsequently progresses through asymptomatic smoldering multiple myeloma (SMM) to symptomatic MM and highly aggressive plasma cell leukemia (PCL) [3–5]. The BM microenvironment plays a crucial role in proliferation, migration, survival and response to drug treatment in MM cells [6]. Therefore, dysregulation of immune microenvironment is one of the hallmarks of MM. Targeting the BM immune microenvironment through immunotherapies, such as monoclonal antibodies daratumumab and elotuzumab, represent promising new treatment options [7–9]. Beside these monoclonal antibodies, other FDA approved therapeutic strategies including immunomodulatory drugs (IMiDs) [10], proteasome inhibitors (e.g. bortezomib, carfilzomib and ixazomib) [11–13] and the combination treatments remarkably improve the overall survival rate. Unfortunately, most patients ultimately suffer from the disease relapse, progression and death, reinforcing the unmet medical need for developing new therapies with novel mechanism of actions (MOA) [2, 14].

Enhancer of zeste homolog 2 (EZH2) is the main catalytic subunit of polycomb repressive complex 2 (PRC2) that silences tumor suppressive gene transcription at the chromatin level at least partly through trimethylation of histone H3 lysine 27 (H3K27me3) [15–17]. Besides the PRC2-dependent catalytic methyltransferase function, EZH2 has diverse noncanonical functions in cancer pathogenesis. For example, EZH2 can interact with RelA/RelB to activate NFκB signaling in estrogen receptor-negative breast cancer [18], bind and methylate transcriptional factor STAT3 to promote tumorigenicity in glioblastoma [19], associate with androgen receptor (AR) to mediate transcriptional activation in castration-resistant prostate cancer (CRPC) [20–22], and associate with the SWI/SNF complex to activate target genes [23]. EZH2 has also been identified by us and others as a coactivator with Myc in driving the development of acute myeloid leukemia (AML) [24], neuroblastoma and small cell lung carcinoma [25], and peripheral T cell lymphoma [26]. Overexpression and aberrant activation of EZH2 have been implicated in a broad variety of human cancers and correlate with poor prognosis [23, 27–29]. Therefore, EZH2 has been pursued as a potential

[1]Mount Sinai Center for Therapeutics Discovery, Departments of Pharmacological Sciences, Oncological Sciences and Neuroscience, Tisch Cancer Institute, Icahn School of Medicine at Mount Sinai, New York, NY 10029, USA. [2]Lineberger Comprehensive Cancer Center, University of North Carolina at Chapel Hill, Chapel Hill, NC 27599, USA. [3]Department of Biochemistry and Biophysics, University of North Carolina at Chapel Hill, Chapel Hill, NC 27599, USA. [4]Department of Genetics, University of North Carolina at Chapel Hill, Chapel Hill, NC 27599, USA. [5]Department of Pharmacology, University of North Carolina at Chapel Hill, Chapel Hill, NC 27599, USA. [6]These authors contributed equally: Xufen Yu, Jun Wang. ✉email: xufen.yu@mssm.edu; greg_wang@med.unc.edu; jian.jin@mssm.edu

Received: 3 October 2022 Revised: 25 January 2023 Accepted: 30 January 2023
Published online: 07 February 2023

therapeutic target. A number of su(var)3-9, enhancer-of-zeste and trithorax (SET) domain-occupying EZH2 inhibitors, including GSK126 [30], EPZ-6438 [31, 32], CPI-1205 [33], PF-06821497 [34], DS-3201 [35], and SHR2554 [36], which potently inhibit the methyltransferase activity of EZH2, have been advanced into clinical investigation. However, to date, EPZ-6438 (Tazemetostat) is the only EZH2 inhibitor approved by the FDA, for the treatment of epithelioid sarcoma and follicular lymphoma.

The aberrant expression and activity of EZH2 are also associated with MM progression [37, 38]. Blockade of the EZH2 methyltransferase activity by catalytic inhibitors has shown some efficacy in suppressing MM cell proliferation [6, 39, 40]. However, the antitumor effect of EZH2 inhibitors in MM is limited, raising the possibility that EZH2 may play additional noncanonical PRC2-independent roles in MM. Proteolysis targeting chimeras (PROTACs), which chemically induce targeted protein degradation (thus both canonical and noncanonical functions of target proteins) through hijacking the ubiquitin-proteasome system (UPS), have emerged as a promising class of therapeutic modalities [41–43]. Previously, we reported an EZH2 PROTAC degrader, MS177, and the therapeutic effect of targeting both canonical and noncanonical functions of EZH2 by MS177 in AML [24]. However, noncanonical functions of EZH2 in MM tumorigenesis are poorly understood, and therapeutic targeting of EZH2's both canonical and noncanonical functions in MM was not explored.

Herein, we report a new noncanonical function of EZH2 in MM, EZH2 interacting with cMyc, co-localizing with gene activation marks and promoting MM tumorigenesis in a PRC2- and H3K27me3-independent manner. We show that both canonical and noncanonical functions of EZH2 in MM cells can be effectively targeted by MS177, an EZH2 degrader, resulting in reactivation of PRC2-repressed genes and immune response genes, and suppression of EZH2-cMyc-mediated oncogenic nodes. Furthermore, MS177, which targets both canonical and noncanonical functions of EZH2, but not C24, an EZH2 catalytic inhibitor that blocks the methyltransferase activity of EZH2 but not noncanonical functions of EZH2, effectively suppressed the in vitro proliferation of multiple MM cell lines. Moreover, MS177, but not C24, effectively inhibited the tumor growth in vivo and improved survival of the treated mice in MM cell line xenograft mouse models. While MS177 was reported previously [24], structure-activity relationship (SAR) studies that led to the discovery of MS177 was not reported. In this study, we also report our SAR study on exploring a variety of linkers, EZH2 binders and E3 ligase binders, which resulted in the discovery of MS177. Overall, we uncovered a new noncanonical function of EZH2 in promoting MM tumorigenesis utilizing an EZH2 degrader, and present pharmacological degradation of EZH2, which targets both canonical and noncanonical functions of EZH2, as a novel therapeutic strategy for the treatment of EZH2-dependent MM.

RESULTS

Discovery of the EZH2 PROTAC MS177, which effectively degrades EZH2/PRC2 in MM cells in a cereblon- and ubiquitination-dependent manner

Previously, we reported that C24 is a highly potent and selective EZH2 inhibitor, which occupies the SET domain of EZH2 with an IC_{50} of 12 ± 2 nM for EZH2 (Fig. 1A) [44]. Using C24 as the EZH2 binding moiety, we previously developed the first EZH2 selective degrader MS1943 using a hydrophobic tagging approach [45]. To develop an EZH2 PROTAC degrader, we conjugated the solvent-exposed piperazinyl group of C24 to pomalidomide (POM), a ligand of the E3 ligase cereblon (CRBN), through a variety of linkers (Fig. 1A). To facilitate installing a linker, we replaced the isopropyl group of C24 with an aminoethyl group (compound 1). We first designed and synthesized a set of EZH2 putative PROTACs **2**–**6** with one to five polyethylene glycol (PEG) units. Their EZH2 degradation effect was examined using immunoblotting at 0.5 and 2.5 μM in L-363 cells, a MM cell line (Fig. 1B). Compound **2** bearing the shortest PEG linker (1 PEG unit) exhibited the most potent EZH2 degradation activity, while compounds **3**–**6** with longer PEG linkers (2–5 PEG units) were generally less effective in inducing EZH2 degradation. Interestingly, reversing the amide moiety in the linker portion (compound **7** versus compound **2**) drastically decreased the EZH2 degradation effectiveness. Similarly, replacing the oxygen atom in the PEG linker with a methylene group (compound **8** versus compound **2**) also diminished the EZH2 degradation effectiveness. These results indicate that the length and composition of the linker moiety play important roles in inducing the target protein degradation [46, 47]. Next, we assessed the effect of employing VHL as the E3 ligase. Compounds **9** and **10** were designed by attaching precursor **1** to VHL-1 [48, 49], which is a well-known VHL E3 ligase recruiting ligand, through the PEG and alkyl linkers of compounds **2** and **8**, respectively. However, compounds **9** and **10** did not effectively degrade EZH2. In addition, we also explored different EZH2 binding moieties, such as GSK126, EPZ-6438, and CPI-1205, using the same linker and CRBN ligand in compound **2**. To our surprise, compounds **11**–**13**, which are derived from these additional EZH2 inhibitors, induced negligible EZH2 degradation (Fig. 1B). We further assessed the anti-proliferative activity of these compounds in L-363 cells. Consistent to their EZH2 degradation effect, only compound **2** effectively suppressed the proliferation of L-363 cells (Supplementary Fig. S1A). Through this SAR study on exploring linkers, E3 ligase recruiting ligands and EZH2 binding moieties, we identified compound **2** (MS177) as the most effective EZH2 degrader in L-363 cells.

Next, we assessed the degradation potency of MS177 in multiple MM cells. We used three control compounds: parental EZH2 inhibitor C24, MS177N1, which is a close analog of MS177 with similar EZH2 inhibitory potency as MS177 but diminished binding to CRBN [24], and MS177N2, another close analog of MS177 which has similar binding affinity to CRBN as MS177 but diminished binding to EZH2 [24](structures of MS177N1 and MS177N2 are shown in Supplementary Fig. S1B). MS177, but not C24, MS177N1 or MS177N2, induced potent EZH2 degradation in MM1.S (another MM line) and L-363 cells in a concentration-dependent manner with half-maximal degradation concentrations (DC_{50}) of 0.6 ± 0.2 and 1.1 ± 0.3 μM, respectively (Fig. 1C–F). In addition, MS177 displayed a similar effect on reducing H3K27me3 compared to C24, while MS177N1 displayed a weaker H3K27me3 inhibition effect (Fig. 1C, E). As expected, MS177N2 did not inhibit H3K27me3, because it contains a modified EZH2 binding moiety designed to abolish EZH2 binding. MS177 also concentration-dependently decreased the protein levels of other two PRC2 core components: suppressor of zeste 12 homolog (SUZ12) and embryonic ectodomain development (EED), in L-363 and MM1.S cells (Supplementary Fig. S1C). Similarly, another essential PRC2 cofactor PHF19 [50] was also degraded in a concentration-dependent manner under the treatment of MS177 (Supplementary Fig. S1D). In addition, the MS177-induced EZH2 degradation effect was also observed in other MM cells, such as U266 and NCI-H929, whereas MS177N1 and C24 did not induce EZH2 reduction (Supplementary Fig. S1E). Furthermore, MS177 induced EZH2 degradation in a time-dependent manner with significant reduction at 16 h, indicating the slow kinetics of MS177-induced EZH2 degradation (Fig. 1G). To verify the mechanism of action (MOA) of MS177-mediated EZH2 degradation, we conducted a series of rescue experiments. Overexpressing of haemagglutinin (HA)-tagged EZH2 SET domain, to which MS177 binds, attenuated the MS177-induced EZH2 and EED depletion in L-363 cells (Fig. 1H). Moreover, EZH2 degradation was effectively blocked by the pretreatment with CRBN ligase ligand POM and Neddy8-activating enzyme (NAE) inhibitor MLN4924 [51], suggesting that

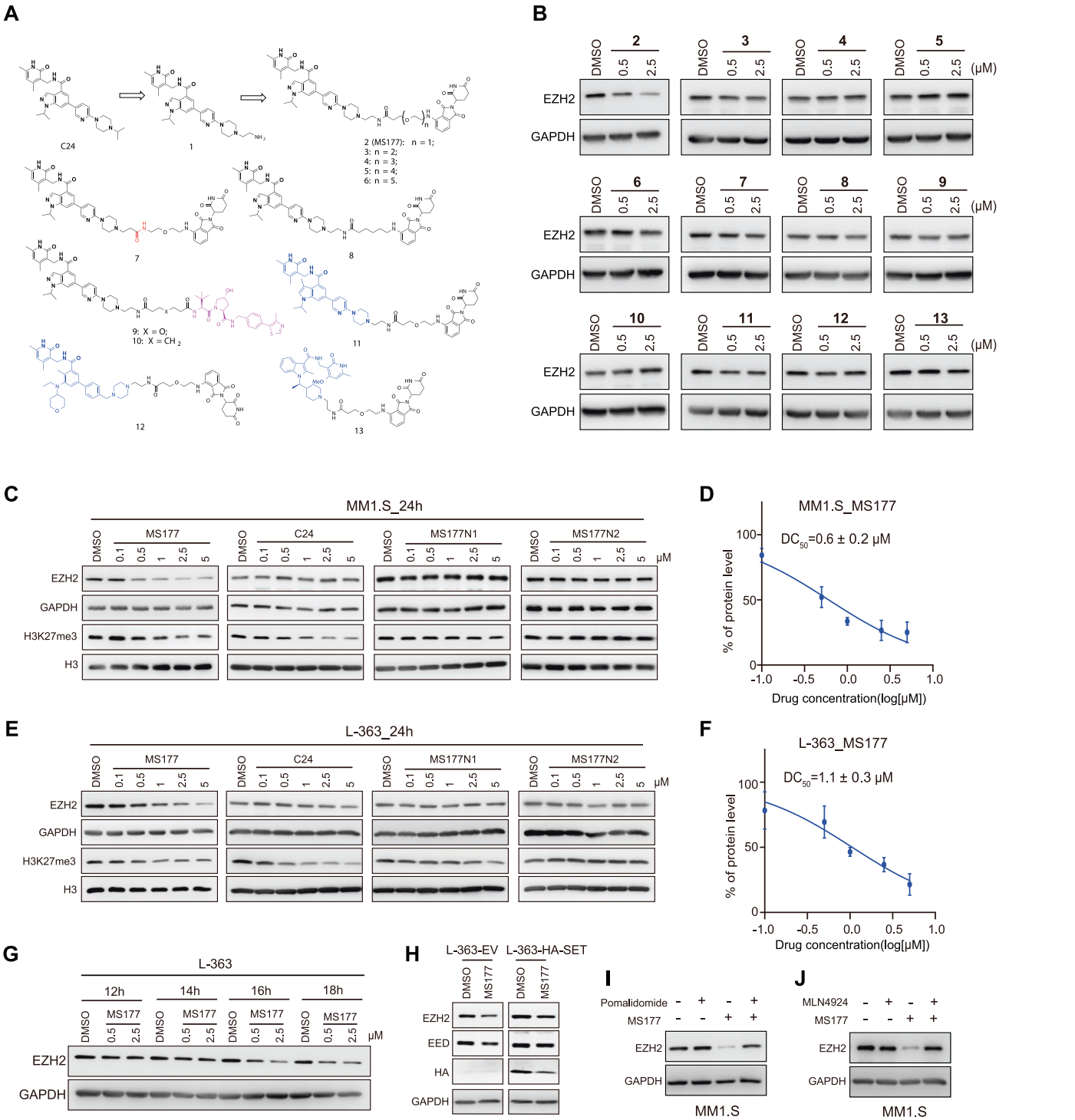

Fig. 1 Design of EZH2 putative degraders 2-13 and their effect on inducing EZH2 protein degradation in L-363 cells. A Chemical structures of compounds **1**–**13**. **B** Immunoblotting showing the EZH2 protein level post-treatment with compounds **2**–**13** at 0.5 and 2.5 μM for 24 h in L-363 cells. DMSO was used as control. Immunoblotting of the protein levels of EZH2 and H3K27me3 in MM1.S (**C**) or L-363 (**E**) cells post-treatment with MS177, C24, MS177N1 or MS177N2 at indicated concentrations versus DMSO, for 24 h. Determination of DC_{50} values of MS177 in MM1.S (**D**) or L-363 (**F**) cells, based on immunoblotting quantifications with ImageJ software from two independent experiments (mean ± S.D.). **G** Time-dependent EZH2 depletion by MS177 (0.5 or 2.5 μM) in L-363 cells. **H** Immunoblotting of the indicated proteins in L-363 cells either stably expressing EV or HA tagged EZH2-SET domain post-treatment of 2.5 μM of MS177 for 24 h. DMSO serves as control. EZH2 immunoblots using MM1.S cells pretreated with DMSO (lanes 1 and 3), pomalidomide (**I**, 2.5 μM, lanes 2 and 4) or MLN4924 (**J**, 0.4 μM, lanes 2 and 4) for 2 h, and then subjected to an additional 14 h treatment with DMSO (lanes 1 and 2) or MS177 (0.5 μM, lanes 3 and 4).

the $CRL4^{CRBN}$ ubiquitin ligase complex is essential for the MS177-induced EZH2 degradation (Fig. 1I–J). Collectively, these results indicate that MS177 effectively induces EZH2 degradation in MM cells in a concentration-, time-, CRBN- and ubiquitination-dependent manner.

We next performed spike-in-controlled Cleavage Under Target and Release Using Nuclease (CUT&RUN) for EZH2 and H3K27me3 in MM1.S cells after treatment with either MS177 or C24. Compared to mock (DMSO) treatment, MS177, but not C24, decreased overall levels of chromatin-bound EZH2, while both compounds suppressed global H3K27me3 (Fig. 2A, B), as exemplified by the changes observed at canonical EZH2-PRC2 target genes, such as *Hox* cluster genes, *CDKN1C* and *UNC5B* (Fig. 2C–E). The drastic reduction in chromatin-bound EZH2 induced by MS177, but not C24, highlights a potential advantage of EZH2 degraders over EZH2 enzymatic inhibitors.

EZH2 noncanonically binds cMyc and co-localizes with gene activation markers in MM cells

We next sought to systematically define genome-wide binding patterns of EZH2 in MM1.S cells by comparing EZH2 and H3K27me3 binding sites using the CUT&RUN technology. A small portion of the EZH2 peaks (4,759 or 19.1%) overlapped with H3K27me3, indicating that these sites are canonical targets of EZH2:PRC2 (Fig. 3A, B; Supplementary Fig. S2A). These EZH2+/H3K27me3+ sites are termed EZH2-ensemble sites. The large portion of EZH2-binding sites (20,100 or 80.9%) lacked H3K27me3 binding (Fig. 3A, B; Supplementary Fig. S2A). These noncanonical EZH2+/H3K27me3- sites are termed EZH2-solo sites. Based on the RNA-sequencing (RNA-seq) data of MM1.S cells [50], the overall expression of the genes associated with EZH2-solo sites was significantly higher than that associated with EZH2-ensemble sites (Supplementary Fig. S2B). Notably, approximately 33% of EZH2-solo sites were localized at gene promoters compared to 21.3% of EZH2-ensemble sites (Supplementary Fig. S2C). Reminiscent of what we observed in AML [24], the E box motif *CACGTG*, a well-known binding motif for cMyc, was also significantly enriched at EZH2-solo sites in MM1.S cells (Fig. 3C). We further verified that EZH2 indeed interacted with cMyc in L-363 cells using co-immunoprecipitation (co-IP) (Fig. 3D). On the genome-wide level, we also observed that the EZH2-solo peaks co-localized with cMyc, Max and a set of gene activation-related markers, including H3K27ac, H3K4me3 and RNA polymerase II (Pol II) (Fig. 3E, top; Supplementary Fig. S2D). This pattern is in stark contrast to what we observed with the EZH2+/H3K27me3+-cobound peaks (Fig. 3E, bottom). Consistently, a significant portion of the EZH2-solo sites overlapped with the binding sites of cMyc (Fig. 3F) and H3K27ac (Supplementary Fig. S2E). These results suggest that EZH2 interacts with cMyc at the EZH2-solo-binding sites, but not canonical EZH2:PRC2 sites, potentially for gene activation.

MS177 targets both EZH2:PRC2 and EZH2:cMyc complexes in MM cells

To dissect the roles of EZH2 at EZH2-solo and EZH2-ensemble target sites in MM cells, we utilized the EZH2 degrader MS177. Compared to DMSO control, MS177 treatment significantly decreased genome-wide binding of EZH2, both at EZH2-ensemble sites and at EZH2-solo sites in the CUT&RUN experiments (Fig. 3G, left). As expected, MS177 treatment also decreased the H3K27me3 level at EZH2-emsemble sites (Fig. 3G, right). Next, we sought to examine the effect of MS177 on the protein level of the EZH2 binding partner cMyc. We found that MS177 induced cMyc degradation in a concentration-dependent manner in L-363 and MM1.S cells, while the control compounds, C24, POM, combination of C24 and POM, MS177N1 and MS177N2, were not able to downregulate cMyc (Fig. 3H, Supplementary Fig. S2F–I). Time-course studies revealed that cMyc was significantly downregulated at 12 h and the maximal degradation was achieved at 18 h (Supplementary Fig. S2G). Notably, MS177 also significantly reduced chromatin-bound levels of EZH2, SUZ12, EED and cMyc, compared to C24 (Supplementary Fig. S2H). Similarly, MS177, but not C24 or MS177N1, effectively reduced the cMyc protein level in other two MM cell lines, U266 and NCI-H299 (Supplementary Fig. S2J). In addition, the MS177-induced cMyc degradation was rescued in L-363 cells with EZH2 knockdown (KD, shEZH2) and knockout (KO, sgEZH2) [45], demonstrating that the cMyc degradation induced by MS177 is dependent on EZH2 (Fig. 3I). Reverse transcription followed by quantitative polymerase chain reaction (RT-qPCR) studies indicated that MS177 treatment did not affect the mRNA levels of cMyc (Fig. 3J). Co-IP experiments further verified that MS177, but not C24, induced the interactions between CRBN and EZH2/cMyc (Fig. 3K). Together, these results suggest that the EZH2 degrader MS177 targets not only the canonical EZH2:PRC2 complex, but also the non-canonical EZH2:cMyc complex for degradation, further supporting that EZH2 degraders are advantageous over EZH2 enzymatic inhibitors.

MS177 suppresses EZH2 and cMyc oncogenic nodes in MM cells

We next determined the transcriptome-modulatory effect of MS177 in MM1.S cells, which were treated with MS177 (with DMSO, C24 and MS177N1 as controls), using RNA-seq (Supplementary Table S1). Compared to DMSO control, dramatic transcriptomic changes were observed only after the treatment with MS177, but not C24 or MS177N1 (Fig. 4A–C). In addition, the MS177-upregulated differentially expressed genes (DEGs) showed negligible degrees of reactivation in response to the comparable treatment of C24 or MS177N1 (Fig. 4D). Therefore, MS177 displayed a superior effect on reactivating PRC2-targeted genes, compared to EZH2 inhibitors. We further compared the MS177-upregulated genes with the published RNA-seq data post-KD of PHF19 [50], an essential PRC2 cofactor. We found a significant overlap of the upregulated genes between MS177 treatment and PHF19 KD, demonstrating that the chemically induced PHF19 degradation by MS177 phenocopied PHF19 genetic KD (Supplementary Fig. S1D and Fig. 4E). In addition, MS177, but not C24 or MS177N1, was able to reactivate PHF19 depressed genes (Fig. 4F). Gene Set Enrichment Analysis (GSEA) revealed that treatment of MS177 reactivated known H3K27me3- or PRC2-repressed genes (Fig. 4G, H). Using RT-qPCR, we confirmed that MS177 significantly reactivated a set of PRC2 associated targets, such as *ATF3*, *DUSP8*, *HOBX7*, *THBS1*, *SMAD7*, *RNF135*, *ANPEP*, and *UNC5B* in MM1.S cells (Supplementary Fig. S3A). C24 treatment, however, did not significantly activate these genes (Supplementary Fig. S3A). We further confirmed the gene-reactivation effect of MS177 was CRBN-dependent through a KO study. MS177 did not effectively reactivate the above PRC2 target genes in CRBN-KO MM1.S cells in general (Supplementary Fig. S3B).

Based on the GSEA, in addition to reactivation of PRC2 target genes (Supplementary Fig. S3C), MS177 also downregulated cMyc-related genes while the control compounds C24 and MS177N1 did not (Fig. 4H, I and Supplementary Fig. S3D, E). Notably, the cMyc binding associated genes were significantly downregulated by MS177, but not C24 or MS177N1 (Fig. 4J). Using RT-qPCR, we further verified that MS177 caused significant downregulation of cMyc target genes, such as *TRAP1*, *E2F1*, *CDC25A* and *PCNA* (Fig. 4K).

Overall, EZH2 degrader MS177, but not EZH2 inhibitor C24 or MS177N1, is effective at both reactivating PRC2–H3K27me3 target genes and suppressing cMyc-associated oncogenes.

MS177 treatment reactivates immune response genes

It has been reported that EZH2 is involved in the modulation of innate immune system and regulates MHC-I or MHC- II antigen processing and presentation pathway [52, 53]. Gene ontology (GO) and GSEA analyses revealed that treatment with MS177, but not C24 or MS177N1, was associated with activation of inflammatory and immune response related pathways, especially

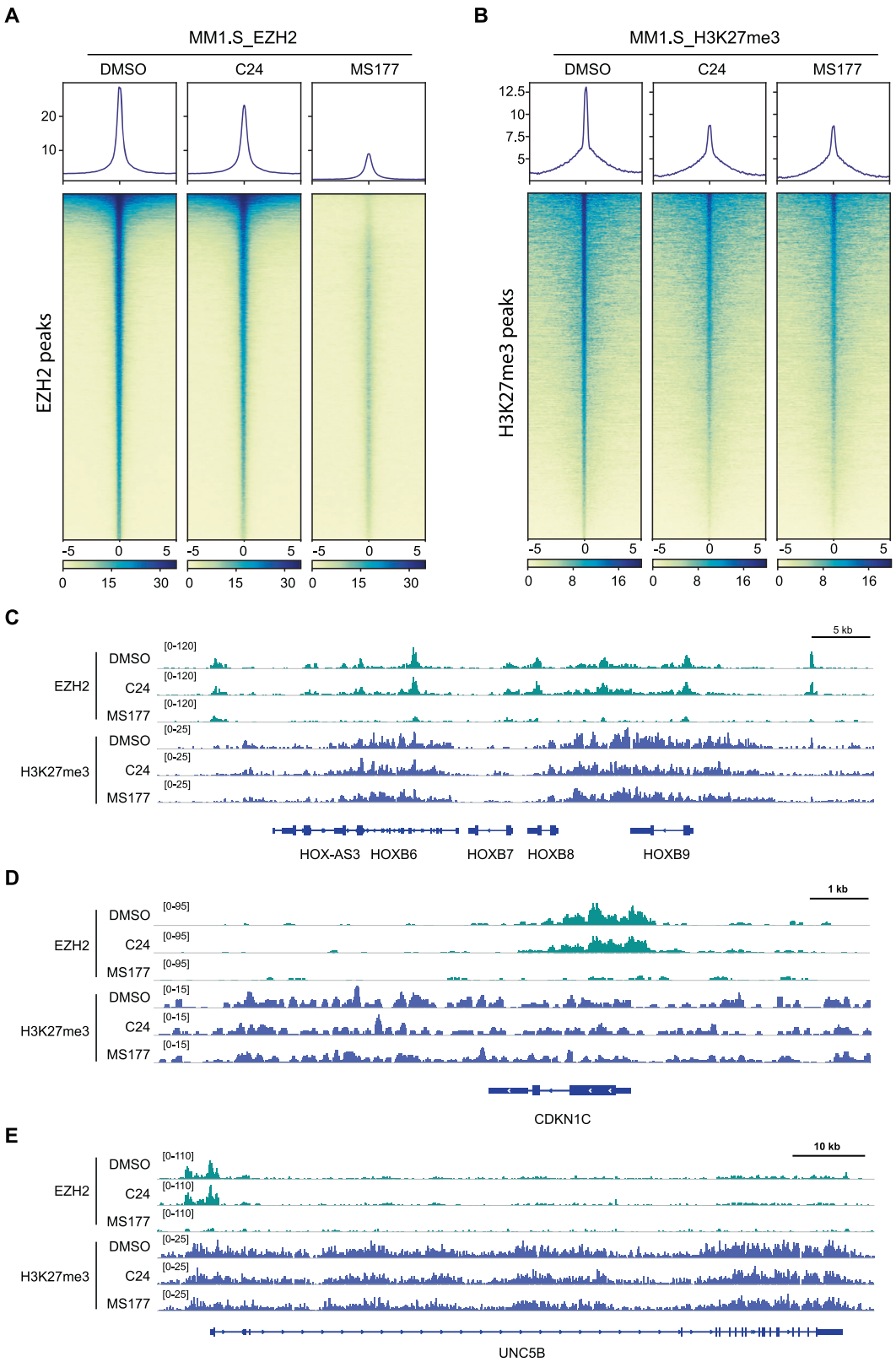

Fig. 2 MS177 decreases genomic binding of both EZH2 and H3K27me3 in MM1.S cells. Average intensities (top panel) and heatmaps (bottom panel) for CUT&RUN signals (normalized against spike-in controls and sequencing depth) of EZH2 and H3K27me3 ± 5 kb around the centers of EZH2 (**A**) and H3K27me3 (**B**) peaks in MM1.S cells post-treatment with DMSO or 2.5 μM of MS177 for 24 h. IGV views of EZH2 and H3K27me3 binding (spike-in control and depth normalized) at *HOXB clusters* (**C**) *CDKN1C* (**D**) or *UNC5B* (**E**) post-treatment of MM1.S cells with DMSO or 2.5 μM of MS177.

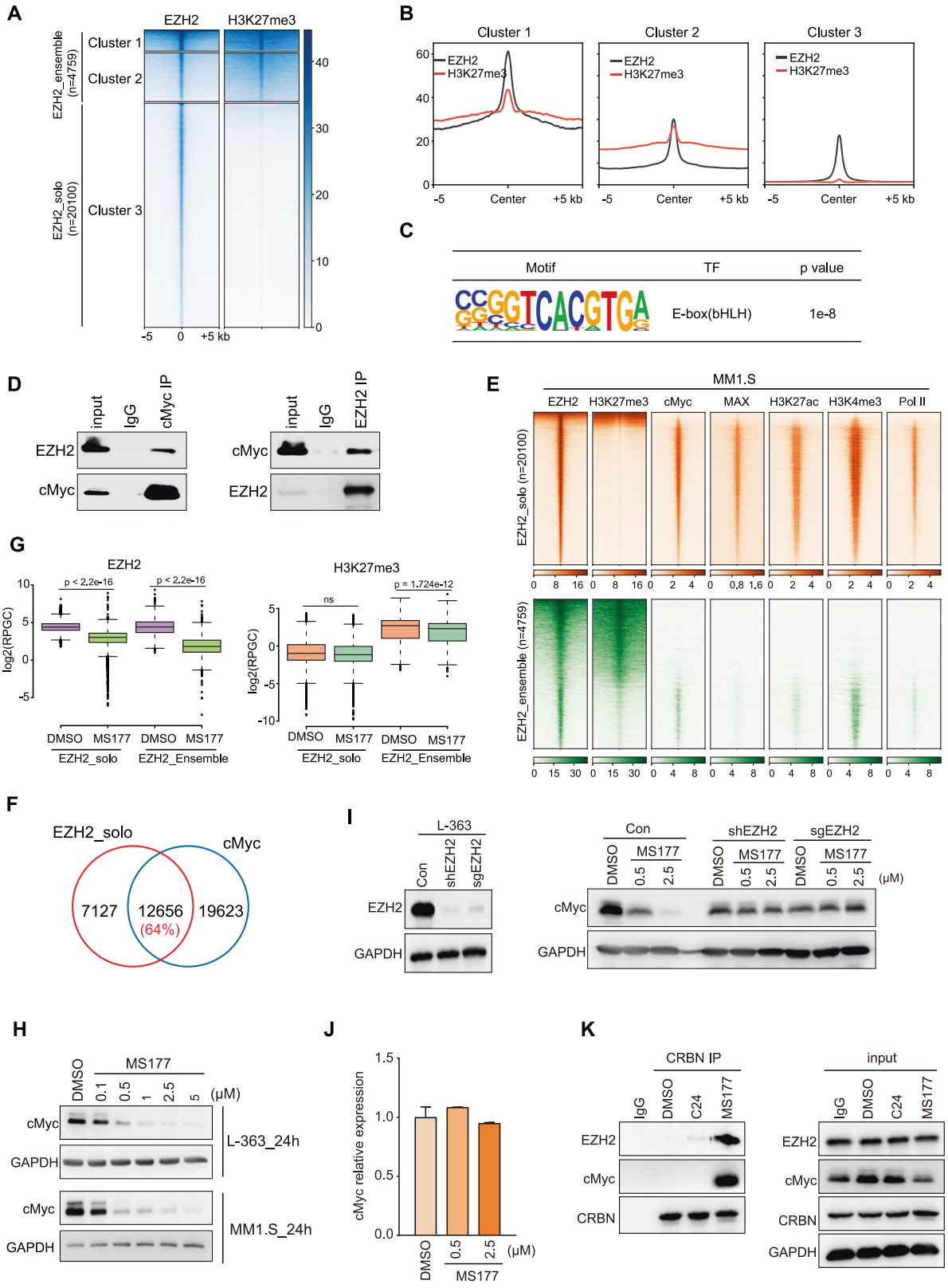

the genes that are involved in interferon-gamma (IFN-γ) response, interferon-α (IFNα) response and MHC antigen processing and presentation in MM1.S cells (Fig. 5A–C, and Supplementary Fig. S4A, B). Moreover, RT-qPCR studies confirmed that MS177, but not C24, significantly activated immune related genes, such as *JAK2*, *TLR4*, *IRF1*, *IRF7*, *IRF8*, *IRF9*, *OAS1* and *OAS3* (Fig. 5D, and Supplementary Fig. S4C). Notably, the activation of these immune related genes was through EZH2 direct regulation. For example, EZH2 and H3K27me3 directly bind *CIITA* and *HLA-DPB* promoters and the binding was significantly decreased with MS177 treatment (Fig. 5E). These data indicate that MS177 is able to reactivate immune response genes in MM cells.

Fig. 3 EZH2 noncanonically interacts with cMyc and co-localizes with gene activation markers in MM cells. A Heatmaps showing the K-means clustered EZH2 and H3K27me3 CUT&RUN signal intensities ±5 kb around peak centers in MM1.S cells. EZH2-'solo' and EZH2-'ensemble' refer to non-canonical EZH2+/H3K27me3− peaks (cluster 3) and canonical EZH2+/H3K27me3+ ones (clusters 1-2), respectively. **B** Averaged EZH2 and H3K27me3 CUT&RUN signals around ±5 kb from the centers of the cluster 1–3 in MM1.S cells. **C** Motif search analysis showing E-box motif enriched in the EZH2-'solo'-binding peaks in MM1.S cells. **D** Co-IP for interactions between endogenous cMyc and EZH2 in L-363 cells. **E** Heatmaps for EZH2, cMyc, MAX, H3K27me3, H3K27ac, H3K4me3 and Pol II ± 5 kb from the center of non-canonical EZH2+H3K27me3– peaks (that is, EZH2-'solo'; top) or canonical EZH2+H3K27me3+ peaks (that is, EZH2-'ensemble'; bottom) in MM1.S cells. With the exception of EZH2 and H3K27me3, which was mapped using CUT&RUN, all the others were mapped using ChIP-seq. **F** Venn diagram showing the overlap of EZH2-'solo' sites with cMyc sites in MM1.S cells. **G** Log2-transformed RPGC counts for CUT&RUN signals of EZH2 (left) and H3K27me3 (right) at those EZH2-'solo' or EZH2-'ensemble' sites identified in MM1.S cells, treated for 24 h with DMSO or 2.5 μM of MS177. The boundaries of box plots indicate the 25th and 75th percentiles, the center line indicates the median, and the whiskers (dashed) indicate 1.5× the interquartile range. Unpaired two-sided t-test. **H** Immunoblotting of cMyc in L-363 (left panel) and MM1.S (right panel) cells after treatment with the indicated concentration of MS177, versus DMSO, for 24 h. **I** EZH2 protein levels (left panel) following EZH2 knockdown (KD; shEZH2) and EZH2 knockout (KO, sgEZH2), relative to empty vector (Con) controls, in L-363 cells. Immunoblotting of cMyc (right panel) in L-363 cells with shEZH2 or sgEZH2 after treatment with the indicated concentration of MS177, or DMSO for 16 h. GAPDH was used as the loading control. **J** RT-qPCR for cMyc gene expression level in L-363 cells, treated with 0.5 and 2.5 μM of MS177 versus DMSO for 16 h. The y-axis shows averaged signals after normalization to GAPDH and to mock-treated samples ($n = 3$; mean ± SD). **K** Co-IP for interactions between CRBN and cMyc and EZH2, respectively, in L-363 cells treated with DMSO, C24 (0.5 μM) and MS177 (0.5 μM) for 12 h by using anti-CRBN antibody for IP. IgG serves as a negative control.

MS177 effectively inhibits cell proliferation in multiple MM cell lines

We first examined the anti-proliferation effect of EZH2 genetic downregulation. EZH2 KD by shRNA (#sh52 and #sh53) significantly inhibited the proliferation of L-363 cells (Supplementary Fig. S5A, B). In addition, EZH2 KD also effectively suppressed the cell proliferation in MM1.S and NCI-H929 cells, respectively (Supplementary Fig. S5C, D). Next, we assessed the anti-proliferative effect of EZH2 degrader MS177, inhibitor C24 and negative control MS177N1 in a panel of MM cell lines, including MM1.S, L-363, U266, NCI-H929, OPM2, KMS-11 and RPMI-8226 (Fig. 6A, B and Supplementary Fig. S6). MS177 potently inhibited the growth of these MM cell lines with GI_{50} values ranging from 0.02 μM to 0.44 μM, which phenocopies the effect of EZH2 KD in L-363, MM1.S and NCI-H929 cells. In contrast, C24 and MS177N1, which inhibit the EZH2 methyltransferase activity and do not induce EZH2 or cMyc degradation, lacked appreciable effects in inhibiting the growth of these MM cell lines (Fig. 6A and Supplementary Figs. S6 and S7A). Notably, CRBN KO remarkably diminished the anti-proliferative activity of MS177 in MM1.S cells, indicating that the MS177-induced anti-proliferative effect is CRBN-dependent (Fig. 6C). Because MS177 is a CRBN-recruiting PROTAC, and Ikaros (IKZF1) and Aiolos (IKZF3) are well known neo-substrates of CRBN [54], we evaluated the effect of MS177 on degrading IKZF1 and IKZF3 in L-363 cells (Fig. 6D). MS177 effectively induced degradation of both IKZF1 and IKZF3. MS177N1, which binds EZH2 but not CRBN, had no effect on degrading IKZF1/3. On the other hand, MS177N2, which binds CRBN but not EZH2, also effectively induced IKZF1/3 degradation. As expected, the EZH2 inhibitor C24 had no effect, but the CRBN ligand pomalidomide (Pom) effectively induced IKZF1/3 degradation. In addition, we assessed the effect of these compounds on inhibiting the L-363 cell proliferation (Fig. 6E). Only MS177 profoundly inhibited the cell growth, while Pom, the combination of Pom with C24 or MS177N2 exhibited mild cell growth inhibition effect. These results suggest that the observed L-363 cell growth inhibition effect is mainly due to MS177-induced degradation of EZH2/cofactors and not IKZF1/3. Moreover, treatment with MS177, but not C24 or MS177N1, effectively inhibited the colony formation of MM1.S (Fig. 6F) and L-363 (Supplementary Fig. S7B) cells. Using fluorescence-activated cell sorting (FACS), we found that MS177, but not C24 or MS177N1, induced cell apoptosis in a concentration-dependent manner (Fig. 6G, H). Induction of apoptosis by MS177, but not C24 or MS177N1, was also confirmed by the significant increase in cleaved-PARP and activation of caspase-3 and -7 induced by MS177 in MM1.S and L-363 (Fig. 6I and Supplementary Fig. S7C). Taken together, these results indicate that EZH2 degrader MS177, but not EZH2 inhibitor C24 or MS177N1, potently suppressed the growth of multiple MM cell lines.

MS177 effectively suppresses the tumor growth in MM xenograft mouse models

Given the profound in vitro anti-proliferative activity of MS177 in multiple MM cell lines, we next assessed the effect of MS177 on inhibiting in vivo tumor growth in a subcutaneous MM1.S xenograft mouse model. Compared to vehicle control, treatment with MS177 at two dosing regimens (100 mg/kg, i.p. BID for 6 days per week; and 200 mg/kg, i.p. BID for 3 days per week) significantly suppressed the tumor growth and prolonged the survival of the treated mice (Fig. 7A, B). In contrast, treatment with C24 at 30 mg/kg, i.p. BID for 6 days per week, a dose which leads to comparable exposure to MS177 based on mouse PK data of C24 [24], showed a much weaker effect on tumor growth inhibition and did not significantly prolong survival (Fig. 7A, B). Furthermore, MS177 also exerted anti-tumor effects (e.g., tumor growth inhibition, survival improvement) in a disseminated MM1.S mouse model (Fig. 7C–E). Lastly, in these in vivo efficacy studies, no obvious body weight changes were observed (Fig. 7F, G), indicating that MS177 was well-tolerated at the tested doses. Overall, these results suggest that EZH2 degraders such as MS177 can inhibit MM tumor growth in vivo without significant toxicity.

DISCUSSION

Canonically, EZH2 and other core components of the PRC2 complex function as an epigenetic silencer of tumor suppressor genes through H3K27me3, the product of PRC2's methyltransferase activity [55, 56]. In addition to this canonical gene silencing function, noncanonical functions of EZH2 have been reported in breast cancer [18], glioblastoma [19], prostate cancer [20–22], acute myeloid leukemia [24], neuroblastoma and small cell lung carcinoma [25], and peripheral T cell lymphoma [26]. However, noncanonical functions of EZH2 in MM have not been reported. In this study, we uncovered that EZH2 binds chromatin at both canonical H3K27me3+ sites (19%) and noncanonical H3K27me3- sites (81%) in MM cells using the CUT&RUN technology. Importantly, EZH2 interacts with cMyc and co-localizes gene activation markers, such as H3K27ac, H3K4me3 and Pol II, at these noncanonical H3K27me3- sites. Notably, both canonical EZH2:PRC2 tumor suppressor gene repression and noncanonical EZH2:cMyc oncogene activation functions are critical contributors to MM development and progression.

EZH2 has been pursued as a promising therapeutic target for treating various cancers [57]. A number of EZH2 small-molecule inhibitors that potently and selectively inhibit the methyltransferase

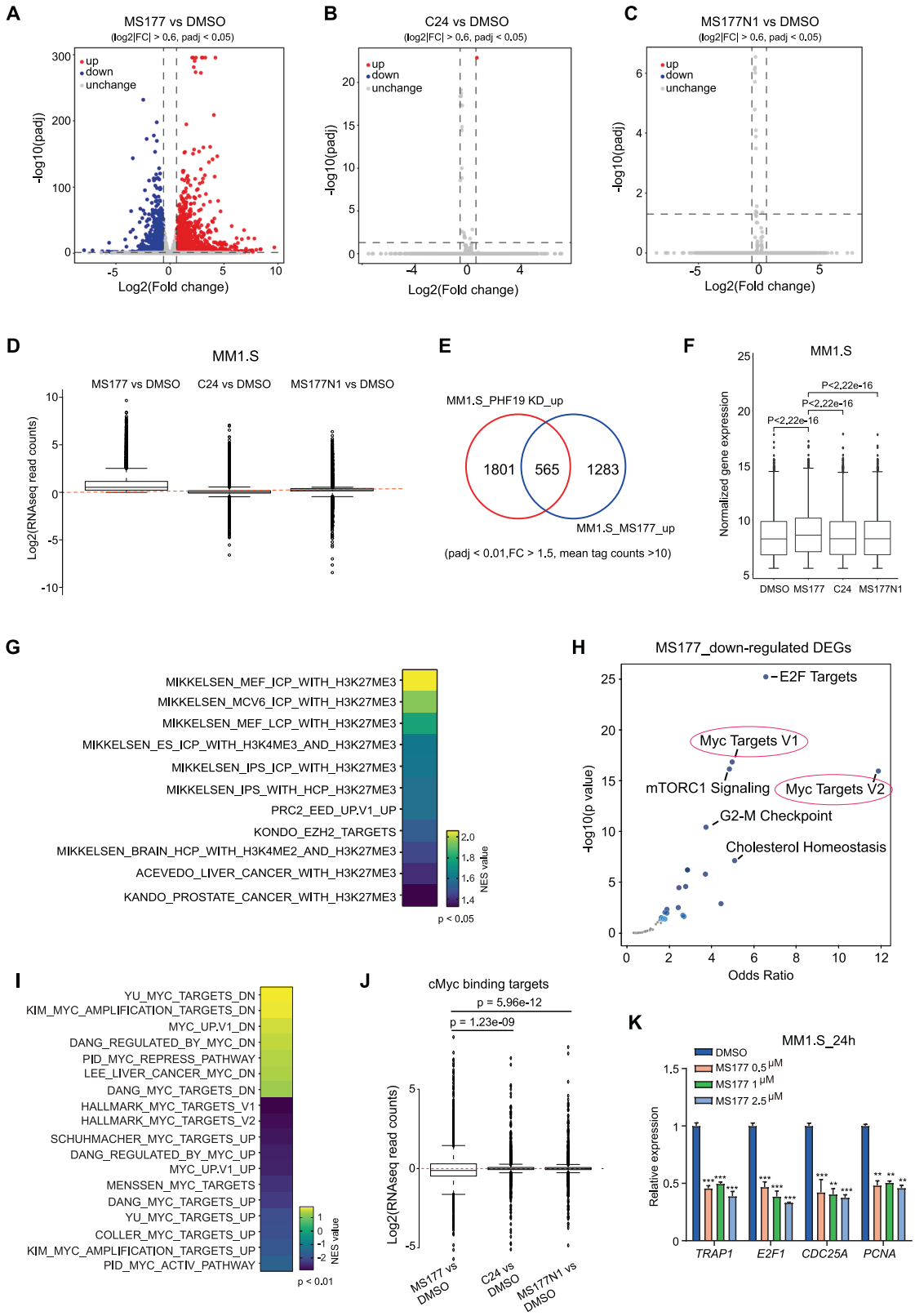

activity of EZH2/PRC2 have been developed [57]. However, EZH2 catalytic inhibitors do not target noncanonical oncogenic functions of EZH2. To target both canonical and noncanonical functions of EZH2, several EZH2 small-molecule degraders have been developed, including MS1943, a hydrophobic tag-based EZH2 degrader [45], MS8815 and YM-281, both of which are VHL-recruiting EZH2 PROTAC degrader [58, 59], and E7, MS177 and U3i, all of which are CRBN-recruiting EZH2 PROTAC degraders [24, 60, 61]. While we reported MS177 previously [24], the detailed SAR study that led to the discovery of MS177 was not reported. In this study, we

Fig. 4 MS177 represses both PRC2 and cMyc-related oncogenic nodes. Volcano plots showing transcriptomic alterations in MM1.S cells following treatment with 0.5 μM of MS177 (**A**), C24 (**B**) or MS177N1 (**C**), compared to DMSO, for 24 h. DEGs with significant expression changes were highlighted. **D** Box plots showing the log2 ratios for DEGs upregulated in MM1.S cells after treatment with MS177 versus DMSO. Comparison was indicated on x-axis, including MS177 vs. DMSO, C24 vs. DMSO, and MS177N1 vs. DMSO. **E** Venn diagram using DEGs upregulated (up) in MM1.S cells after treatment of MS177 and those after PHF19 knock-down (KD) relative to DMSO. **F** Boxplot showing the mean vst normalized expression of the PHF19-repressed transcripts in MM1.S cells, after treatment with 0.5 μM of DMSO, MS177, C24 or MS177N1 for 24 h ($n = 2$). EZH2-repressed genes are defined in **E** after PHF19 KD versus DMSO. The boundaries of box plots indicate the 25th and 75th percentiles, the center line indicates the median, and the whiskers (dashed) indicate 1.5× the interquartile range. Paired two-sided t-test was used. *P* value were adjusted for multiple testing using the bonferroni correction. **G** Heatmap of GSEA normalized enrichment score (NES) values revealing that MS177 treatment is highly correlated with de-repression of the PRC2- or H3K27me3-repressed genes. **H** The volcano plot shows the enrichment of MSigDB gene sets for the downregulated DEGs by MS177 treatment in MM1.S cells. Each point represents a single gene set; the x-axis measures the odds ratio (0, inf) calculated for the gene set, while the y-axis indicates the -log (p value) of the gene set. Larger blue points represent significant terms (p value < 0.05); smaller gray points represent non-significant terms. **I** Summary of GSEA results showing the correlation of the indicated Myc-related gene sets with MS177 treatment relative to mock. Yellow and blue in the heatmap indicate positive and negative correlations, respectively. **J** Box plots showing the log2 ratios for DEGs bound by cMyc in MM1.S cells. Comparison was indicated on x-axis, including MS177 vs. DMSO, C24 vs. DMSO, and MS177N1 vs. DMSO. The boundaries of box plots indicate the 25th and 75th percentiles, the center line indicates the median, and the whiskers (dashed) indicate 1.5× the interquartile range. Unpaired two-sided t-test was used. **K** RT-qPCR of cMyc-mediated upregulated targets in MM1.S cells after treatment with indicated concentrations of MS177 for 24 h. The y axis shows signals after normalization to DMSO-treated cells ($n = 3$; mean ± S.D.; unpaired two-tailed t-test). *, **, and *** denote $P < 0.05$, 0.01 and 0.005, respectively. NS denotes not significant.

described our SAR results from investigating the effect of various linkers, E3 ligase binders and EZH2 ligands on degrading EZH2 in MM cells. This detailed SAR study culminated in the discovery of MS177.

Importantly, we demonstrated that both canonical and non-canonical oncogenic functions of EZH2 in MM cells can be effectively targeted by EZH2 degraders such as MS177 in this study. In particular, MS177 effectively degraded both EZH2:PRC2 and EZH2:cMyc complexes in a concentration-, time-, CRBN-, EZH2- and ubiquitination-dependent manner, leading to reactivation of PRC2-repressed genes and suppression of EZH2-cMyc-mediated oncogenic nodes in MM cells. Moreover, MS177, but not EZH2 catalytic inhibitors, reactivated immune response genes in MM cells, which raised the possibility that EZH2 degraders could elicit more profound antitumor effects in immunocompetent models. Furthermore, MS177, but not the parent EZH2 catalytic inhibitor C24 or its negative control MS177N1, effectively suppressed the proliferation of multiple MM cell lines. Lastly, MS177, but not C24, significantly inhibited the tumor growth in vivo and improved survival without apparent toxicity in MM xenograft mouse models. A limitation of these in vivo efficacy studies is that immunodeficient mice were used in the studies. Therefore, the potential antitumor effects mediated through MS177's ability in reactivating immune response genes were not assessed in these models. Future studies using syngeneic mouse models are warranted. Collectively, our results suggest that pharmacological degradation of EZH2, which effectively targets both canonical and non-canonical functions of EZH2, as a novel therapeutic strategy is superior to pharmacological inhibition of EZH2 for the treatment of MM.

METHODS

Compound synthesis and chemical characterization

MS177 (**2**), C24, MS177N1 and MS177N2 were synthesized and used as reported previously [24]. The synthesis and characterization of compounds **3**–**13** are described in Supplementary Materials.

Cell lines

293 T cells were obtained from American Tissue Culture Collection (ATCC, CRL-3216). Human hematological cancer cell lines used in the study include a panel of multiple myeloma cell lines MM1.S (ATCC, CRL-2974), L-363 (DSMZ, ACC49), NCI-H929 (ATCC, CRL-9068), OPM2 (DSMZ, ACC50), U266 (ATCC, TIB-196), RPMI-R8226 (ATCC, CRM-CCL-155), and KMS-11 (a gift of KC Anderson). These lines were cultured according to vendor's specifications. MM1.S-T11, a MM1.S derivative line with knockout (KO) of the E3 ligase CRBN, was a kind gift of Drs. J Brander and W Kaelin (DFCI). To generate luciferase-labeled cell line, cells were spin-infected with Mscv-luciferase-IRES-neo retrovirus and selected with 1 mg/mL Geneticin (Gibco). Luciferase expression was validated with Luciferase Assay System (Promega).

Antibodies

Antibodies used in the work include mouse anti-EZH2 (BD, Cat # 612666), Sheep anti-EED (R&D, Cat # AF5827), rabbit anti-H3 (Abcam, Cat # ab1791), rabbit anti-EZH2 (Cell Signaling Technology (CST), Cat # 5246), rabbit anti-cMyc (CST, Cat # 5605), rabbit anti-H3K27me3 (CST, Cat # 9733), rabbit anti-HA tag (CST, Cat # 3724), rabbit anti-GAPDH (CST, Cat # 5174), rabbit anti-SUZ12 (Abcam, Cat # ab12073), rabbit anti-PHF19 (CST, Cat # 77271), rabbit anti-IKZF1 (CST, Cat # 9034), rabbit anti-IKZF3 (CST, Cat # 15103), rabbit anti-CRBN (CST, Cat # 71810), rabbit anti-PARP (CST, Cat # 9532), rabbit anti-Cleaved Caspase-3 (CST, Cat # 9661), rabbit anti-Cleaved Caspase-7 (CST, Cat # 8438). Normal Rabbit IgG (CST, Cat # 2729). HRP-linked secondary antibodies, either anti-mouse IgG (Cat # 7076) or anti-rabbit IgG (Cat # 7074), were obtained from Cell Signaling Technology. Sheep IgG HRP-conjugated Antibody (R&D, Cat # HAF016) were used as secondary antibody.

Cleavage Under Targets & Release Using Nuclease (CUT&RUN)

CUT&RUN was performed as previously described [24]. Briefly, 0.5 million of cells were first collected, washed in the CUT&RUN wash buffer, and then bound to the activated ConA beads (Bangs Laboratories, #BP531). Next, the cell:bead sample was incubated with antibodies against the protein target (1:100 dilution) and then permeabilized in the digitonin-containing buffer, which was then followed by washing in the digitonin buffer, incubation with pAG-MNase, and another washing in the digitonin buffer to remove the unbound pAG-MNase. After the final wash, cells were subjected to digestion following the pAG-MNase activation by addition of the pAG-MNase digestion buffer, followed by incubation on rotator for 2 h at 4 °C. Solubilized chromatin was then released using the CUT&RUN stop buffer, in which equal amount of Drosophila spike-in chromatin (0.5 ng/sample) was added for spike-in normalization, and DNA purification was carried out with the PCR cleanup kit. About 1–5 ng of the purified CUT&RUN DNA was used for preparation of multiplexed libraries with the NEB Ultra II DNA Library Prep Kit per manufacturer's instruction. Sequencing was conducted using an Illumina NextSeq 500 Sequencing System.

ChIP-seq and CUT&RUN data analysis

ChIP-seq data downloaded from GEO were re-analyzed as previously described [24]. For CUT&RUN, raw reads were mapped to the reference genome (hg19) using bowtie v2.3.5. The non-primary alignment, PCR duplicates, or blacklist regions were removed from aligned data by Samtools (v1.9), Picard 'MarkDuplicates' function (v2.20.4), and bedtools (v2.28.0), respectively. Peak calling was performed using MACS2 (macs2 callpeak -f BAMPE -g hs/mm –keep-dup 1). Deeptools (v3.3.0) was used to generate bigwig files. Genomic binding profiles were generated using the deepTools 'bam-Compare' functions. Profiles of CUT&RUN or ChIP-seq read densities were displayed in Integrative Genomics Viewer (IGV, Broad

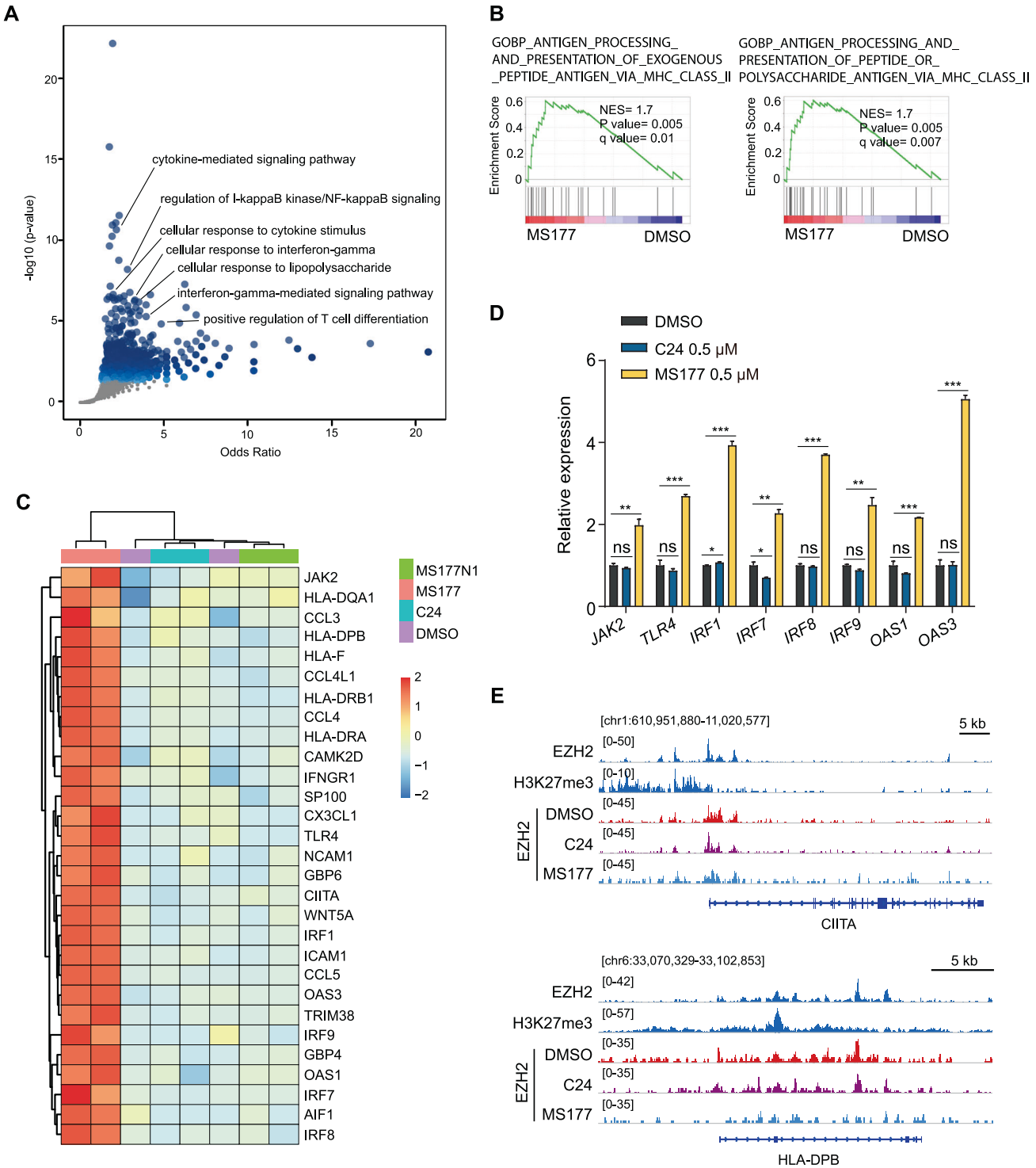

Fig. 5 MS177 treatment reactivates immune response genes. A The volcano plot showing Gene Ontology (GO) analysis of the up-regulated DEGs by MS177 treatment in MM1.S cells. Each point represents a single gene set; the x-axis measures the odds ratio (0, inf) calculated for the gene set, while the y-axis gives the -log(p-value) of the gene set. Larger blue points represent significant terms (p value < 0.05); smaller gray points represent non-significant terms. Immune related pathways are indicated. **B** GSEA showing that, relative to controls, MS177 treatment in MM1.S cells are positively correlated with upregulation of the MHC class II presenting-related gene sets. **C** Heatmap showing immune related gene expression changes in MM1.S cells after MS177, C24, or MS177N1 treatment compared to DMSO. **D** RT-qPCR for immune response genes in MM1.S cells after the treatment of 0.5 mM of C24 and MS177, respectively, for 24 h. Y-axis shows signals after normalization to DMSO-treated cells ($n = 3$; mean ± SD; unpaired two-tailed Student's t test). *, **, and *** denote $P < 0.05$, 0.01 and 0.005, respectively. ns denotes not significant. **E** IGV views of H3K27me3 and EZH2 binding (spike-in control and depth normalized) at *CIITA* or *HLA-DPB* post-treatment with DMSO or 2.5 μM of MS177 for 24 h in MM1.S cells.

A

Cell lines	cancer types	EC_{50} (μM)		
		MS177	C24	MS177N1
MM1.S	MM	0.02	>100	>100
L-363	MM	0.07	4	12
U266	MM	0.04	6	>100
NCI-H929	MM	0.02	20	48
OPM2	MM	0.27	20	>100
KMS-11	MM	0.44	NA	NA
RPMI-8226	MM	0.18	NA	NA

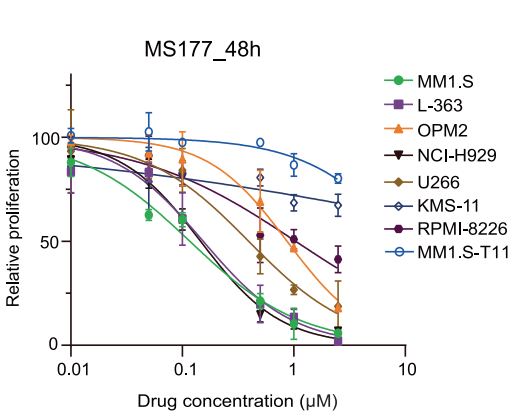

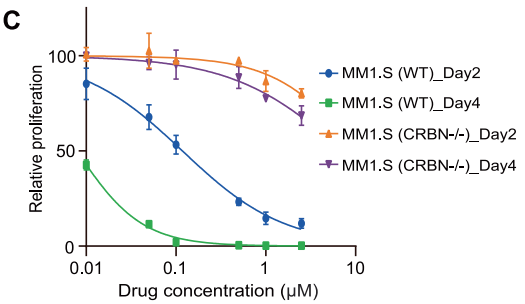

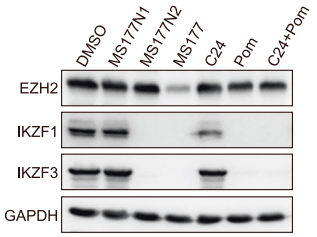

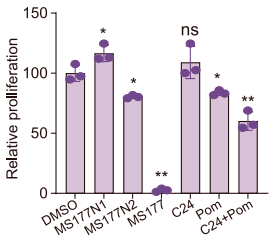

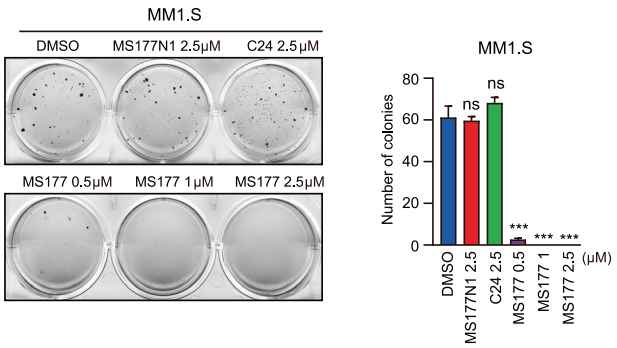

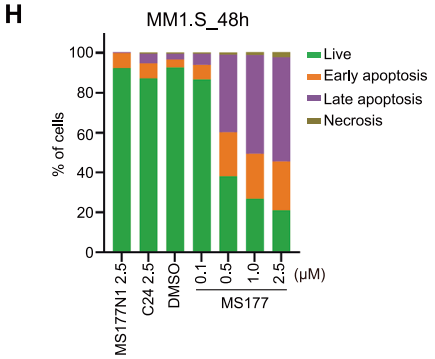

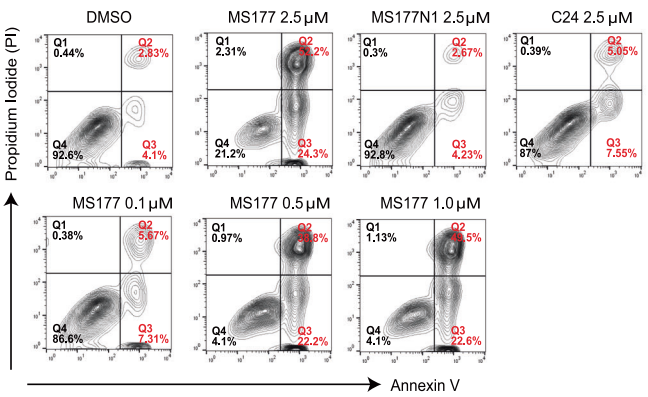

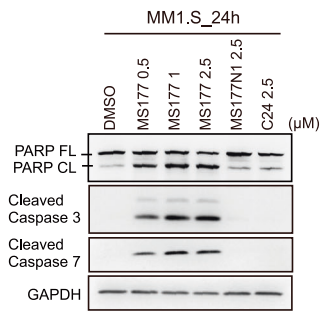

Institute). Heatmaps for ChIP-seq signals were generated using the deepTools "computeMatrix" and "plotHeatmap" functions. The enrichment of motifs was identified by the software HOMER [62] with default parameters.

RNA-seq and data analysis

RNA-seq was performed as described [24, 63]. Total RNA was first purified using RNeasy Plus Mini Kit (Qiagen, #74136) and then treated with Turbo DNA-free kit (Thermo, #AM1907) to remove genomic DNA. Multiplexed RNA-seq libraries were subjected for deep sequencing. Reads were mapped to the reference genome followed by analysis of differentially

Fig. 6 MS177 effectively inhibits the growth of MM cells. A EC_{50} values of MS177, C24 and MS177N1 in a panel of MM cell lines after 4 days of treatment ($n = 3$). **B** Plots showing the growth inhibitory effects of MS177 at indicated concentrations (x-axis; in the log10 converted values) in the indicated MM cells after 2-day treatment. Y-axis shows relative growth after normalization to DMSO-treated cells ($n = 3$; mean ± S.D.). **C** Plots showing the growth inhibitory effects of MS177 at indicated concentrations (x-axis; in the log10 converted values) in either wild-type (WT) or CRBN-/- MM1.S cells after 2-day or 4-day treatment. Y-axis shows relative growth after normalization to DMSO-treated cells ($n = 3$; mean ± S.D.). **D** Immunoblotting of the protein levels of EZH2, IKZF1 and IKZF3 in L-363 cells post-treatment with MS177N1, MS177N2, MS177, C24, pomalidomide (Pom) or the combination of C24 and Pom at 2.5 mM versus DMSO, for 24 h. **E** Growth inhibitory effect of DMSO, MS177N1, MS177N2, MS177, C24, Pom and the combination of C24 and Pom (x-axis) at 2.5 mM in the L-363 cells after 2-day treatment. Y-axis shows relative growth after normalization to DMSO-treated cells ($n = 3$; mean ± SD; unpaired two-tailed Student's *t* test). *, **, and *** denote $P < 0.05$, 0.01 and 0.005, respectively. NS denotes not significant. **F** Representative views of soft agar-based assay (left panel) and quantifications of colony formation (right panel; colony numbers counted by ImageJ and presented in average ± S.D. of two independent experiments) of MM1.S cells post-treatment with DMSO, 2.5 μM of MS177N1 or C24, or three indicated concentrations (0.5, 1, or 2.5 μM) of MS177. *, **, and *** denote $P < 0.05$, 0.01 and 0.005, respectively. ns denotes not significant. Unpaired two-tailed Student's *t* test. **G**, **H** Apoptosis analysis after a 24-h treatment with the indicated compounds in MM1.S cells. **I** Immunoblotting for the indicated apoptotic markers in MM1.S cells, treated with either 2.5 μM of MS177N1 or C24 or indicated concentrations (0.5, 1, or 2.5 μM) of MS177, compared to DMSO, for 24 h.

expressed genes (DEG) as before [63, 64]. Fastq files were aligned to the GRCh37 (hg19) human genome using STAR v2.4.2 [65] with parameters: --outSAMtype BAM Unsorted --quantMode TranscriptomeSAM. Transcript abundance was estimated with salmon v0.1.19 [66] to quantify the transcriptome defined by Gencode v22. Gene level counts were summed across isoforms and genes with low counts (maximum expression <10) were filtered for the downstream analyses. Raw read counts were used for differential gene expression analysis by DESeq2 v1.38.2 [67] where size normalization factor was estimated based on median-of-ratios. GSEA [68] was performed as described [24]. Expression heatmaps were generated using mean-centered log2 converted TPM (Transcripts Per Million) sorted in descending order based on expression values in R's package "gplots" v3.0.3 with either no clustering or column hierarchical clustering by average linkage. Volcano plots visualizing DEGs were produced using R's package "EnhancedVolcano" v3.11. Annotation of DEGs was conducted using Metascape [69].

Plasmid construction and transfection

The SET domain (aa612-738) of EZH2 was cloned from GST-EZH2 (Gift of Dr. Haojie Huang), fused with a HA tag, and then cloned into a lentivirus vector pCDH-EF1a-MCS-IRES-puro (System Biosciences). 293 T cells were seeded in 100 mm dish and transfected on the next day with PEI (sigma) following manufacturer's instructions. Cells were harvested 48 h after transfection for analysis such as co-IP or blotting.

Gene knockdown (KD) and knockout (KO)

The pLKO.1 lentiviral shRNA plasmid for knockdown of EZH2 were obtained from Sigma. Teton-inducible EZH2 KD was used as before [22]. CRISPR-V2 based EZH2 KO was used as previously described [45]. All plasmids used are verified by sequencing. Target sequences for EZH2 shRNAs were as follows:

EZH2 shRNA (sh52): TATGATGGTTAACGGTGATCA.
EZH2 shRNA (sh53): GAAACAGCTGCCTTAGCTTCA.

Viral production and stable cell line generation

Lentiviruses were prepared with the packaging system in 293 T cells. In brief, 293 T cells were co-transfected with lentiviral vector and the packaging plasmids (psPAX2 and pMD 2.5 G) and the supernatant containing viruses were harvested at 48- and 72-h post-transfection. After filtration with 0.45-μm filters, viruses were used to infect target cells in the presence of 8 μg/mL polybrene. 48 h post-infection, cells were selected with either 1 μg/mL of puromycin (Gibco) or 1 mg/mL of Geneticin (Gibco) for 7 days to establish stable expression cell lines.

Cell fractionation

1 million cells were harvested, washed with cold PBS, and resuspended in 200 μL of CSK buffer (10 mM Pipes pH 7.0, 300 mM sucrose, 100 mM NaCl, 3 mM $MgCl_2$, 0.1% Triton X-100, freshly supplemented with protease/phosphatase inhibitor cocktail), followed by incubation on ice for 30 min, as described [24]. Then, the sample was subject to centrifugation at 1300 × *g* for 5 mins at 4 °C to collect supernatant (which contains soluble proteins) and pellet fractions (which contains the chromatin-associated proteins). Cell pellets were dissolved in 1.5× SDS loading buffer. Same amounts of protein sample were used for immunoblotting.

Immunoblotting (IB)

Cells were collected and lysed in EBC buffer (50 mM Tris pH 8.0, 120 mM NaCl, 0.5% NP40, 0.1 mM EDTA, and 10% glycerol) freshly supplemented with a complete protease inhibitor cocktail (Roche) and phosphatase inhibitor (Roche). Protein concentration of cell lysates was measured by Bradford assay (BioRad). Equal amounts of protein lysates were separated by SDS-PAGE and transferred to PVDF membranes (Millipore). Quantification of the intensity of protein bands by normalizing to GAPDH was performed by ImageJ software.

Co-immunoprecipitation (co-IP)

IP was performed as described previously [24, 70]. Cell pellets were lysed in EBC buffer (freshly supplemented with protease/phosphatase inhibitors) on ice for 30 min. After sonication, debris was removed by centrifugation at 12,000 × *g* for 15 min at 4 °C. 1 mg of proteins from whole cell lysate was incubated with antibodies against target proteins overnight at 4 °C, followed by addition of 10 μL of protein A or G magnetic beads (BioRad) and rotation for an additional 3 h at 4 °C. Bound complexes were centrifuged, washed with EBC buffer for three times, and subjected to SDS-PAGE and immunoblotting.

Reverse transcription followed by quantitative polymerase chain reaction (RT-qPCR)

RNA was isolated using the RNeasy PLUS Mini Kit (Qiagen). RT was performed with 1 ug of total RNA using cDNA Reverse Transcription kit according to the manufacturer's protocols (Invitrogen), followed by qPCR using SYBR Green Master Mix (BioRad) on a QuantStudio 6 Flex Real-Time PCR System (Thermo). The relative abundance of gene expression was calculated using the comparative CT method which compares the Ct value of target gene to that of GAPDH. Primers for RT-qPCR are listed as follows: JAK2-RT-F (AGAATGTCTTGGGATGGCAG); JAK2-RT-R (TGATAG TCTTGGATCTTTGCTCG); OAS1-RT-F (CATCTGTGGGTTCCTGAAGG); OAS1-RT-R (GAGAGGACTGAGGAAGACAAC); OAS3-RT-F (TCTGAGTAGAGACGGG ACATC); OAS3-RT-R (TGGGCTGGAGAAATTCACTG); TLR4-RT-F (AGTTGATCT ACCAAGCCTTGAGT); TLR4-RT-R (GCTGGTTGTCCCAAAATCACTTT); IRF1-RT-F (AGTGATCTGTACAACTTCCAGG); IRF1-RT-R (CCTTCCTCATCCTCATCTGT TG); IRF7-RT-F (TCCCCACGCTATACCATCTAC); IRF7-RT-R (GAAGACACACCC TCACGC); IRF8-RT-F (AAGTTACAGAGATGGAGTGCG); IRF8-RT-R (CATCCCC ATGTAATCGTCCAC); IRF9-RT-F (CTTGGTCAGGTACTTTCAGGG); IRF9-RT-R (AGCAAGTATCGGGCAAAGG). Other primers used for RT-qPCR are used as before [24].

Cell growth inhibition assay

Cell growth inhibition assay was performed as described previously [24, 71]. In brief, cells were seeded in each well of 24-well plates in triplicates, subjected to treatment of compounds added in various final concentrations. Fresh medium containing compounds were changed every two days. All flowing cell cultures were periodically diluted to keep a cell density of less than 1×10^6/mL at all times. Cell numbers were counted by an automated TC10 cell counter (BioRad) every two days. EC_{50} (The effective control to 50% growth inhibition) values were calculated using a nonlinear regression analysis of the mean ± S.D. from at least triplicated datasets for each biological assay.

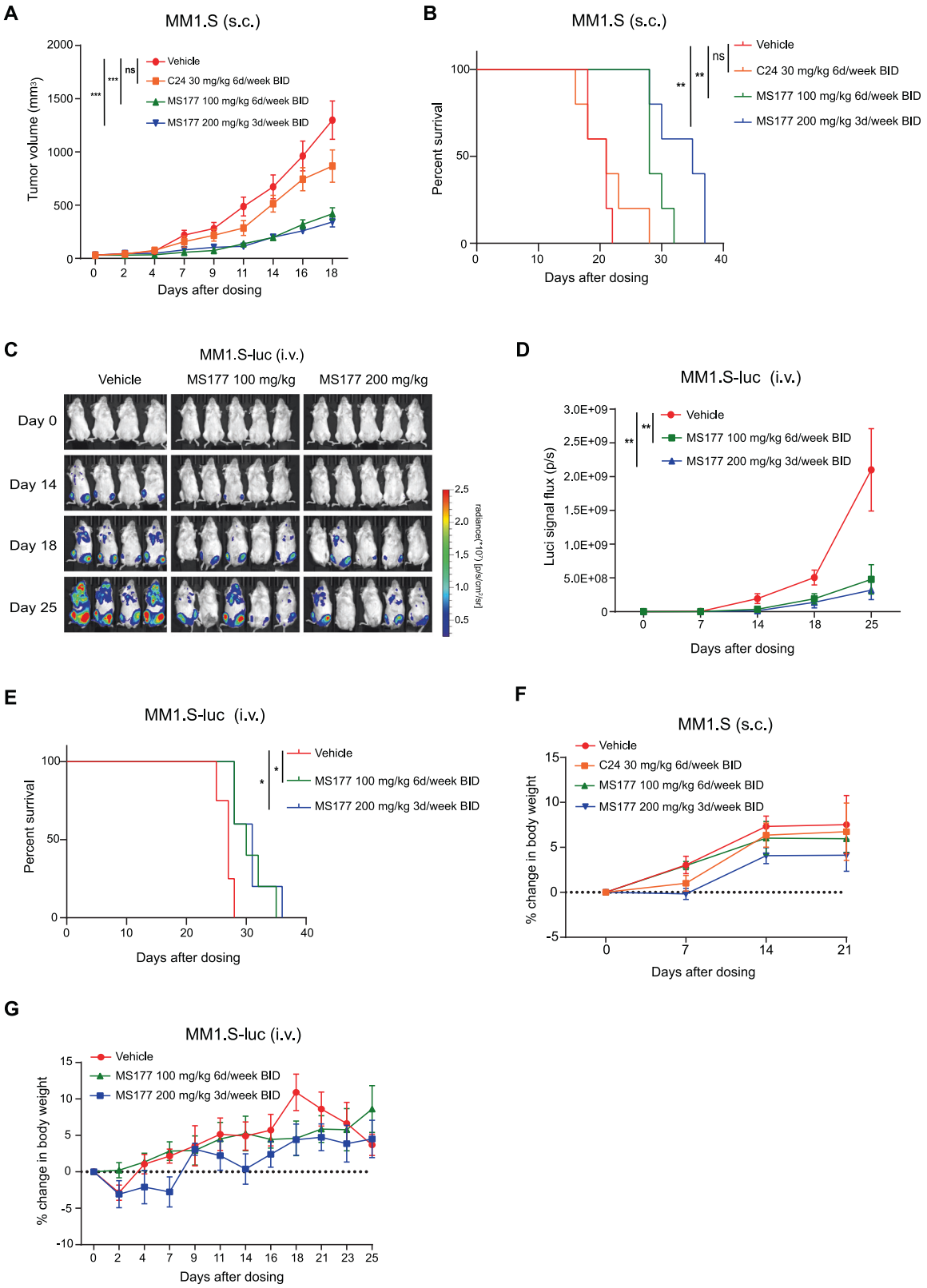

Fig. 7 MS177 suppresses MM tumor growth in vivo. Averaged tumor volume (**A**) and Kaplan–Meier curve (**B**) of MM1.S subcutaneous (s.c.) xenograft mouse models after treatment with vehicle, MS177 or C24 at indicated dosage ($n = 5$ per group; mean ± S.D.). Statistical significance was determined by two-way ANOVA (**A**), log-rank (Mantel–Cox, **B**) test. Bioluminescent images (**C**), signal levels (**D**) and Kaplan–Meier curves (**E**) of NSG mice transplanted intravenously (i.v.) with the luciferase-labeled MM1.S cells after treatment with vehicle or the indicated MS177 dosage ($n = 5$ per group; mean ± S.D.). Statistical significance was determined by two-way analysis of variance (ANOVA; **D**) or log-rank (Mantel–Cox, **E**) test. Body weight change of NSG mice bearing the MM1.S tumors, xenografted either subcutaneously (s.c.; **F**) or intravenously (i.v.; **G**), as measured from the starting time point of treatment with the indicated dose of vehicle or MS177 over a course of 21 or 25 days (mean ± S.D.).

Annexin V apoptosis assay

For measurement of apoptosis, cells were collected after treatment, washed with cold PBS and stained with Annexin V-FITC Apoptosis Detection Kit (BD) following the manufacturer's instructions. Apoptosis was detected with a CyAnADP flow cytometer, and then analyzed by FlowJo Software (BD).

Soft agar colony formation assay

Soft agar-based colony formation assay was performed as described previously. Briefly, cells were plated at a density of 12,000 cells/mL for L-363 cells and 24,000 cells/mL for MM1.S cells in complete medium supplemented with 0.4% of agarose onto the bottom layers composed of medium with 1% of agarose. Every four days, 0.5 mL of fresh complete media containing compound was added onto the plate. After 3-4 weeks' incubation, cell culture plates were stained with 100 μg/mL of iodonitrotetrazoliuim chloride solution (sigma), and after incubation overnight, numbers of cell colonies were counted.

Subcutaneous human tumor models

All animal experiments were approved by and conducted in accord with guidelines of Institutional Animal Care and Use Committee at UNC. NOD/SCID/IL2Rgammanull (NSG) mice were acquired from the Jackson Laboratory. Mice were housed in a germ-free environment with food and tap water ad libitum. Room temperature and relative humidity were held at 22 ± 2 °C and 30–70%, respectively. Automatic light control guaranteed a 12-h light/dark cycle (7:00 to 19:00/19:00 to 7:00). MS177 was dissolved for in vivo use as previously described [24]. 5 million MM1.S cells were suspended in 100 μL of DPBS with 50% Matrigel (Corning) and then injected subcutaneous (s.c.) in the bilateral flank of NSG mice. Tumor volume (mm^3) = (length × $width^2$)/2 and was measured using electronic calipers three times per week. Once tumors reached an average of approximately 50–100 mm^3, animals were randomized into groups ($n = 5$ per group) such that the average tumor volume at the beginning of treatment administration was uniform across treatment groups. Animals were then i.p. dosed with MS177 at 100 mg/kg two times a day (BID) for 6 days/week, 200 mg/kg BID for 3 days/week or C24 at 30 mg/kg BID for 6 days/week. Clinical signs were monitored every day. Mice body-weight changes and tumor volume were measured 3×/week until study termination.

Orthotopic human tumor models

The luciferase labeled MM1.S were injected intravenously (i.v.) into the tail vein of NSG mice. In vivo MM growth was monitored via weekly chemiluminescence imaging of mice following intraperitoneal injection with D-luciferin. Once tumors reached an average Bioluminescence imaging (BLI) of 1×10^5 photons/second, animals were randomized into groups ($n = 5$ per group) such that the average BLI signals at the beginning of treatment administration was uniform across treatment groups. Animals were then i.p. administered MS177 at 100 mg/kg two times a day (BID) for 6 days/week or 200 mg/kg BID for 3 days/week. Clinical signs, body-weight changes, and tumor BLI were measured 2 times per week until study termination.

Statistics and reproducibility

Statistical analyses were performed using GraphPad Prism (version 9). Unpaired two-tailed Student's *t* test was used for experiments comparing two sets of data with assumed normal distribution. Data are presented as mean ± S.D. from at least three independent experiments. *, **, and *** denote the *P* value of <0.05, 0.01 and 0.005, respectively. $P < 0.05$ was considered to be statistically significant. NS denotes not significant. No statistical methods were used to predetermine sample size. All data from representative experiments (such as imaging and micrographs) were repeated at least two times independently with similar results.

DATA AVAILABILITY

Genomic dataset of this study, including CUT&RUN and RNA-Seq, have been deposited in NCBI Gene Expression Omnibus (GEO) database under accession code GSE214669. Publicly available datasets used in the work were from NCBI GEO accession numbers GSE36354 (cMyc, MAX, H3K27ac, H3K4me3 and Pol II data in MM1.S cells). Other data supporting the findings of this study are available upon request.

CODE AVAILABILITY

We did not use custom code. All software and packages used in this study are listed in Reporting Summary and are publicly available.

REFERENCES

1. Cowan AJ, Green DJ, Kwok M, Lee S, Coffey DG, Holmberg LA, et al. Diagnosis and Management of Multiple Myeloma: A Review. JAMA. 2022;327:464–77.
2. van de Donk NWCJ, Pawlyn C, Yong KL. Multiple myeloma. Lancet. 2021;397:410–27.
3. Kuehl WM, Bergsagel PL. Multiple myeloma: evolving genetic events and host interactions. Nat Rev Cancer. 2002;2:175–87.
4. Kyle RA, Therneau TM, Rajkumar SV, Offord JR, Larson DR, Plevak MF, et al. A long-term study of prognosis in monoclonal gammopathy of undetermined significance. N Engl J Med. 2002;346:564–9.
5. Morgan GJ, Walker BA, Davies FE. The genetic architecture of multiple myeloma. Nat Rev Cancer. 2012;12:335–48.
6. Hernando H, Gelato KA, Lesche R, Beckmann G, Koehr S, Otto S, et al. EZH2 inhibition blocks multiple myeloma cell growth through upregulation of epithelial tumor suppressor genes. Mol Cancer Ther. 2016;15:287–98.
7. D'Agostino M, Innorcia S, Boccadoro M, Bringhen S. Monoclonal antibodies to treat multiple myeloma: a dream come true. Int J Mol Sci. 2020;21:8192.
8. Krejcik J, Frerichs KA, Nijhof IS, van Kessel B, van Velzen JF, Bloem AC, et al. Monocytes and granulocytes reduce CD38 expression levels on myeloma cells in patients treated with daratumumab. Clin Cancer Res. 2017;23:7498–511.
9. Krejcik J, Casneuf T, Nijhof IS, Verbist B, Bald J, Plesner T, et al. Daratumumab depletes CD38+ immune regulatory cells, promotes T-cell expansion, and skews T-cell repertoire in multiple myeloma. Blood. 2016;128:384–94.
10. Quach H, Ritchie D, Stewart AK, Neeson P, Harrison S, Smyth MJ, et al. Mechanism of action of immunomodulatory drugs (IMiDS) in multiple myeloma. Leukemia. 2010;24:22–32.
11. Manasanch EE, Orlowski RZ. Proteasome inhibitors in cancer therapy. Nat Rev Clin Oncol. 2017;14:417–33.
12. Moreau P, Richardson PG, Cavo M, Orlowski RZ, San Miguel JF, Palumbo A, et al. Proteasome inhibitors in multiple myeloma: 10 years later. Blood. 2012;120:947–59.
13. Ge M, Qiao Z, Kong Y, Liang H, Sun Y, Lu H, et al. Modulating proteasome inhibitor tolerance in multiple myeloma: an alternative strategy to reverse inevitable resistance. Br J Cancer. 2021;124:770–6.
14. D'Agostino M, Bertamini L, Oliva S, Boccadoro M, Gay F. Pursuing a curative approach in multiple myeloma: a review of new therapeutic strategies. Cancers. 2019;11:2015.
15. Kaniskan HU, Martini ML, Jin J. Inhibitors of protein methyltransferases and demethylases. Chem Rev. 2018;118:989–1068.
16. Comet I, Riising EM, Leblanc B, Helin K. Maintaining cell identity: PRC2-mediated regulation of transcription and cancer. Nat Rev Cancer. 2016;16:803–10.
17. Wang J, Wang GG. No easy way out for EZH2: its pleiotropic, noncanonical effects on gene regulation and cellular function. Int J Mol Sci. 2020;21:9501.
18. Gonzalez ME, DuPrie ML, Krueger H, Merajver SD, Ventura AC, Toy KA, et al. Histone methyltransferase EZH2 induces Akt-dependent genomic instability and BRCA1 inhibition in breast cancer. Cancer Res. 2011;71:2360–70.
19. Kim E, Kim M, Woo DH, Shin Y, Shin J, Chang N, et al. Phosphorylation of EZH2 activates STAT3 signaling via STAT3 methylation and promotes tumorigenicity of glioblastoma stem-like cells. Cancer Cell. 2013;23:839–52.
20. Xu K, Wu ZJ, Groner AC, He HH, Cai C, Lis RT, et al. EZH2 oncogenic activity in castration-resistant prostate cancer cells is Polycomb-independent. Science. 2012;338:1465–9.
21. Kim J, Lee Y, Lu X, Song B, Fong KW, Cao Q, et al. Polycomb- and methylation-independent roles of EZH2 as a transcription activator. Cell Rep. 2018;25:2808–2820 e2804.
22. Wang J, Park KS, Yu X, Gong W, Earp HS, Wang GG, et al. A cryptic transactivation domain of EZH2 binds AR and AR's splice variant, promoting oncogene activation and tumorous transformation. Nucleic Acids Res. 2022;50:10929–46.
23. Kim KH, Kim W, Howard TP, Vazquez F, Tsherniak A, Wu JN, et al. SWI/SNF-mutant cancers depend on catalytic and non-catalytic activity of EZH2. Nat Med. 2015;21:1491–6.
24. Wang J, Yu X, Gong W, Liu X, Park KS, Ma A, et al. EZH2 noncanonically binds cMyc and p300 through a cryptic transactivation domain to mediate gene activation and promote oncogenesis. Nat Cell Biol. 2022;24:384–99.
25. Wang L, Chen C, Song Z, Wang H, Ye M, Wang D, et al. EZH2 depletion potentiates MYC degradation inhibiting neuroblastoma and small cell carcinoma tumor formation. Nat Commun. 2022;13:12.
26. Vanden Bempt M, Debackere K, Demeyer S, Van Thillo Q, Meeuws N, Fernandez CP, et al. Aberrant MYCN expression drives oncogenic hijacking of EZH2 as a transcriptional activator in peripheral T cell lymphoma. Blood. 2022;140:2463–76.

27. Varambally S, Dhanasekaran SM, Zhou M, Barrette TR, Kumar-Sinha C, Sanda MG, et al. The polycomb group protein EZH2 is involved in progression of prostate cancer. Nature. 2002;419:624–9.
28. Bachmann IM, Halvorsen OJ, Collett K, Stefansson IM, Straume O, Haukaas SA, et al. EZH2 expression is associated with high proliferation rate and aggressive tumor subgroups in cutaneous melanoma and cancers of the endometrium, prostate, and breast. J Clin Oncol. 2006;24:268–73.
29. Herrera-Merchan A, Arranz L, Ligos JM, de Molina A, Dominguez O, Gonzalez S. Ectopic expression of the histone methyltransferase Ezh2 in haematopoietic stem cells causes myeloproliferative disease. Nat Commun. 2012;3:623.
30. McCabe MT, Ott HM, Ganji G, Korenchuk S, Thompson C, Van Aller GS, et al. EZH2 inhibition as a therapeutic strategy for lymphoma with EZH2-activating mutations. Nature. 2012;492:108–12.
31. Knutson SK, Wigle TJ, Warholic NM, Sneeringer CJ, Allain CJ, Klaus CR, et al. A selective inhibitor of EZH2 blocks H3K27 methylation and kills mutant lymphoma cells. Nat Chem Biol. 2012;8:890–6.
32. Knutson SK, Warholic NM, Wigle TJ, Klaus CR, Allain CJ, Raimondi A, et al. Durable tumor regression in genetically altered malignant rhabdoid tumors by inhibition of methyltransferase EZH2. Proc Natl Acad Sci USA. 2013;110:7922–7.
33. Vaswani RG, Gehling VS, Dakin LA, Cook AS, Nasveschuk CG, Duplessis M, et al. Identification of (R)-N-((4-Methoxy-6-methyl-2-oxo-1,2-dihydropyridin-3-yl) methyl)-2-methyl-1-(1-(1 -(2,2,2-trifluoroethyl)piperidin-4-yl)ethyl)-1H-indole-3-carboxamide (CPI-1205), a potent and selective inhibitor of histone methyltransferase EZH2, suitable for phase I clinical trials for B-cell lymphomas. J Med Chem. 2016;59:9928–41.
34. Kung PP, Bingham P, Brooun A, Collins M, Deng YL, Dinh D, et al. Optimization of orally bioavailable enhancer of zeste homolog 2 (EZH2) inhibitors using ligand and property-based design strategies: identification of development candidate (R)-5,8-Dichloro-7-(methoxy(oxetan-3-yl)methyl)-2-((4-methoxy-6-methyl-2-oxo-1,2- dihydropyridin-3-yl)methyl)-3,4-dihydroisoquinolin-1(2H)-one (PF-06821497). J Med Chem. 2018;61:650–65.
35. Honma D, Nosaka E, Shiroishi M, Takata Y, Hama Y, Yamamoto Y, et al. DS-3201, a potent EZH1/2 dual inhibitor, demonstrates antitumor activity against non-Hodgkin lymphoma (NHL) regardless of EZH2 mutation. Blood. 2018;132:2217–2217.
36. Wang X, Wang D, Ding N, Mi L, Yu H, Wu M, et al. The synergistic anti-tumor activity of EZH2 inhibitor SHR2554 and HDAC inhibitor chidamide through ORC1 reduction of DNA replication process in diffuse large B cell lymphoma. Cancers. 2021;13:4249.
37. Croonquist PA, Van, Ness B. The polycomb group protein enhancer of zeste homolog 2 (EZH 2) is an oncogene that influences myeloma cell growth and the mutant ras phenotype. Oncogene. 2005;24:6269–80.
38. Pawlyn C, Bright MD, Buros AF, Stein CK, Walters Z, Aronson LI, et al. Overexpression of EZH2 in multiple myeloma is associated with poor prognosis and dysregulation of cell cycle control. Blood Cancer J. 2017;7:e549.
39. Nylund P, Atienza Parraga A, Haglof J, De Bruyne E, Menu E, Garrido-Zabala B, et al. A distinct metabolic response characterizes sensitivity to EZH2 inhibition in multiple myeloma. Cell Death Dis. 2021;12:167.
40. Alzrigat M, Parraga AA, Agarwal P, Zureigat H, Osterborg A, Nahi H, et al. EZH2 inhibition in multiple myeloma downregulates myeloma associated oncogenes and upregulates microRNAs with potential tumor suppressor functions. Oncotarget. 2017;8:10213–24.
41. Dale B, Cheng M, Park KS, Kaniskan HU, Xiong Y, Jin J. Advancing targeted protein degradation for cancer therapy. Nat Rev Cancer. 2021;21:638–54.
42. Bekes M, Langley DR, Crews CM. PROTAC targeted protein degraders: the past is prologue. Nat Rev Drug Disco. 2022;21:181–200.
43. Li K, Crews CM. PROTACs: past, present and future. Chem Soc Rev. 2022;51:5214–36.
44. Yang X, Li F, Konze KD, Meslamani J, Ma A, Brown PJ, et al. Structure-activity relationship studies for enhancer of zeste homologue 2 (EZH2) and Enhancer of Zeste Homologue 1 (EZH1) inhibitors. J Med Chem. 2016;59:7617–33.
45. Ma A, Stratikopoulos E, Park KS, Wei J, Martin TC, Yang X, et al. Discovery of a first-in-class EZH2 selective degrader. Nat Chem Biol. 2020;16:214–22.
46. Yu X, Xu J, Xie L, Wang L, Shen Y, Cahuzac KM, et al. Design, synthesis, and evaluation of potent, selective, and bioavailable AKT kinase degraders. J Med Chem. 2021;64:18054–81.
47. Yu X, Xu J, Shen Y, Cahuzac KM, Park KS, Dale B, et al. Discovery of potent, selective, and in vivo efficacious AKT kinase protein degraders via structure-activity relationship studies. J Med Chem. 2022;65:3644–66.
48. Zengerle M, Chan KH, Ciulli A. Selective small molecule induced degradation of the BET bromodomain protein BRD4. ACS Chem Biol. 2015;10:1770–7.
49. Raina K, Lu J, Qian Y, Altieri M, Gordon D, Rossi AM, et al. PROTAC-induced BET protein degradation as a therapy for castration-resistant prostate cancer. Proc Natl Acad Sci USA. 2016;113:7124–9.
50. Ren Z, Ahn JH, Liu H, Tsai YH, Bhanu NV, Koss B, et al. PHF19 promotes multiple myeloma tumorigenicity through PRC2 activation and broad H3K27me3 domain formation. Blood. 2019;134:1176–89.
51. Soucy TA, Smith PG, Milhollen MA, Berger AJ, Gavin JM, Adhikari S, et al. An inhibitor of NEDD8-activating enzyme as a new approach to treat cancer. Nature. 2009;458:732–6.
52. Ennishi D, Takata K, Beguelin W, Duns G, Mottok A, Farinha P, et al. Molecular and genetic characterization of MHC deficiency identifies EZH2 as therapeutic target for enhancing immune recognition. Cancer Disco. 2019;9:546–63.
53. Burr ML, Sparbier CE, Chan KL, Chan YC, Kersbergen A, Lam EYN, et al. An evolutionarily conserved function of polycomb silences the MHC Class I antigen presentation pathway and enables immune evasion in cancer. Cancer Cell. 2019;36:385–401 e388.
54. Kronke J, Udeshi ND, Narla A, Grauman P, Hurst SN, McConkey M, et al. Lenalidomide causes selective degradation of IKZF1 and IKZF3 in multiple myeloma cells. Science. 2014;343:301–5.
55. Gan L, Yang Y, Li Q, Feng Y, Liu T, Guo W. Epigenetic regulation of cancer progression by EZH2: from biological insights to therapeutic potential. Biomark Res. 2018;6:10.
56. Tremblay-LeMay R, Rastgoo N, Pourabdollah M, Chang H. EZH2 as a therapeutic target for multiple myeloma and other haematological malignancies. Biomark Res. 2018;6:34.
57. Bhat KP, Umit Kaniskan H, Jin J, Gozani O. Epigenetics and beyond: targeting writers of protein lysine methylation to treat disease. Nat Rev Drug Disco. 2021;20:265–86.
58. Dale B, Anderson C, Park K-S, Kaniskan HÜ, Ma A, Shen Y, et al. Targeting triple-negative breast cancer by a novel proteolysis targeting chimera degrader of enhancer of Zeste homolog 2. ACS Pharmacol Transl Sci. 2022;5:491–507.
59. Tu Y, Sun Y, Qiao S, Luo Y, Liu P, Jiang ZX, et al. Design, synthesis, and evaluation of VHL-based EZH2 degraders to enhance therapeutic activity against lymphoma. J Med Chem. 2021;64:10167–84.
60. Liu Z, Hu X, Wang Q, Wu X, Zhang Q, Wei W, et al. Design and synthesis of EZH2-based PROTACs to degrade the PRC2 complex for targeting the noncatalytic activity of EZH2. J Med Chem. 2021;64:2829–48.
61. Wang C, Chen X, Liu X, Lu D, Li S, Qu L, et al. Discovery of precision targeting EZH2 degraders for triple-negative breast cancer. Eur J Med Chem. 2022;238: 114462.
62. Ahn JH, Davis ES, Daugird TA, Zhao S, Quiroga IY, Uryu H, et al. Phase separation drives aberrant chromatin looping and cancer development. Nature. 2021;595:591–5.
63. Cai L, Tsai YH, Wang P, Wang J, Li D, Fan H, et al. ZFX mediates non-canonical oncogenic functions of the androgen receptor splice variant 7 in castrate-resistant prostate cancer. Mol Cell. 2018;72:341–354 e346.
64. Yu X, Li D, Kottur J, Shen Y, Kim HS, Park KS, et al. A selective WDR5 degrader inhibits acute myeloid leukemia in patient-derived mouse models. Sci Transl Med. 2021;13:eabj1578.
65. Dobin A, Davis CA, Schlesinger F, Drenkow J, Zaleski C, Jha S, et al. STAR: ultrafast universal RNA-seq aligner. Bioinformatics. 2013;29:15–21.
66. Patro R, Duggal G, Love MI, Irizarry RA, Kingsford C. Salmon provides fast and bias-aware quantification of transcript expression. Nat Methods. 2017;14:417–9.
67. Love MI, Huber W, Anders S. Moderated estimation of fold change and dispersion for RNA-seq data with DESeq2. Genome Biol. 2014;15:550.
68. Subramanian A, Tamayo P, Mootha VK, Mukherjee S, Ebert BL, Gillette MA, et al. Gene set enrichment analysis: a knowledge-based approach for interpreting genome-wide expression profiles. Proc Natl Acad Sci USA. 2005;102:15545–50.
69. Zhou Y, Zhou B, Pache L, Chang M, Khodabakhshi AH, Tanaseichuk O, et al. Metascape provides a biologist-oriented resource for the analysis of systems-level datasets. Nat Commun. 2019;10:1523.
70. Liu X, Simon JM, Xie H, Hu L, Wang J, Zurlo G, et al. Genome-wide screening identifies SFMBT1 as an oncogenic driver in cancer with VHL loss. Mol Cell. 2020;77:1294–1306 e1295.
71. Xu B, On DM, Ma A, Parton T, Konze KD, Pattenden SG, et al. Selective inhibition of EZH2 and EZH1 enzymatic activity by a small molecule suppresses MLL-rearranged leukemia. Blood. 2015;125:346–57.

ACKNOWLEDGEMENTS

We graciously thank the Wang and Jin Laboratory members for helpful discussion and technical support. This work was supported in part by the US National Institutes of Health grants R01CA218600 (to JJ and GGW), R01CA268519 (GGW and JJ) and R01CA230854 (to JJ), an endowed professorship from the Icahn School of Medicine at Mount Sinai (to JJ), and grants/awards from Gabrielle's Angel Foundation for Cancer Research (to GGW), When Everyone Survives (WES) Leukemia Research Foundation (to GGW) and UNC Lineberger Cancer Center UCRF Stimulus Initiative Grants (to GGW and LC). GGW is an American Cancer Society Research Scholar, a Leukemia and Lymphoma Society Scholar, and an American Society of Hematology Scholar in Basic Science. This work utilized the NMR Spectrometer Systems at Mount Sinai acquired with funding from National Institutes of Health SIG grants 1S10OD025132 and

1S10OD028504. We thank UNC's facilities, including High-throughput Sequencing Facility (HTSF), Bioinformatics Core, Tissue Culture Facility, Animal Studies Core and UNC Tissue Procurement Facility, for their professional assistance of this work. The cores affiliated to the UNC Cancer Center are supported in part by the UNC Lineberger Comprehensive Cancer Center Core Support Grant P30CA016086.

AUTHOR CONTRIBUTIONS

JW, XY, AM, YS, CZ and XL led on biological/genomic and chemical biology studies, respectively, under the guidance of GGW and JJ. JW and WG conducted RNA-seq data analysis under the supervision of LC and GGW. JW analyzed the CUT&RUN and ChIP-seq data under the direction of GGW. XY, JW, LC, JL, GGW and JJ analyzed and interpreted experimental data. JJ and GGW conceived the project. JJ and GGW organized and led the study. XY, WJ, GGW and JJ wrote the manuscript with input from all other authors.

COMPETING INTERESTS

The Jin laboratory received research funds from Celgene Corporation, Levo Therapeutics, Inc., Cullgen, Inc. and Cullinan Oncology, Inc. JJ is a cofounder and equity shareholder in Cullgen, Inc., a scientific cofounder and scientific advisory board member of Onsero Therapeutics, Inc., and a consultant for Cullgen, Inc., EpiCypher, Inc. and Accent Therapeutics, Inc. The other authors declare no competing interests.

ADDITIONAL INFORMATION

Supplementary information The online version contains supplementary material available at https://doi.org/10.1038/s41388-023-02618-5.

Correspondence and requests for materials should be addressed to Xufen Yu, Gang Greg Wang or Jian Jin.